CHALMERS
UNIVERSITY OF TECHNOLOGY

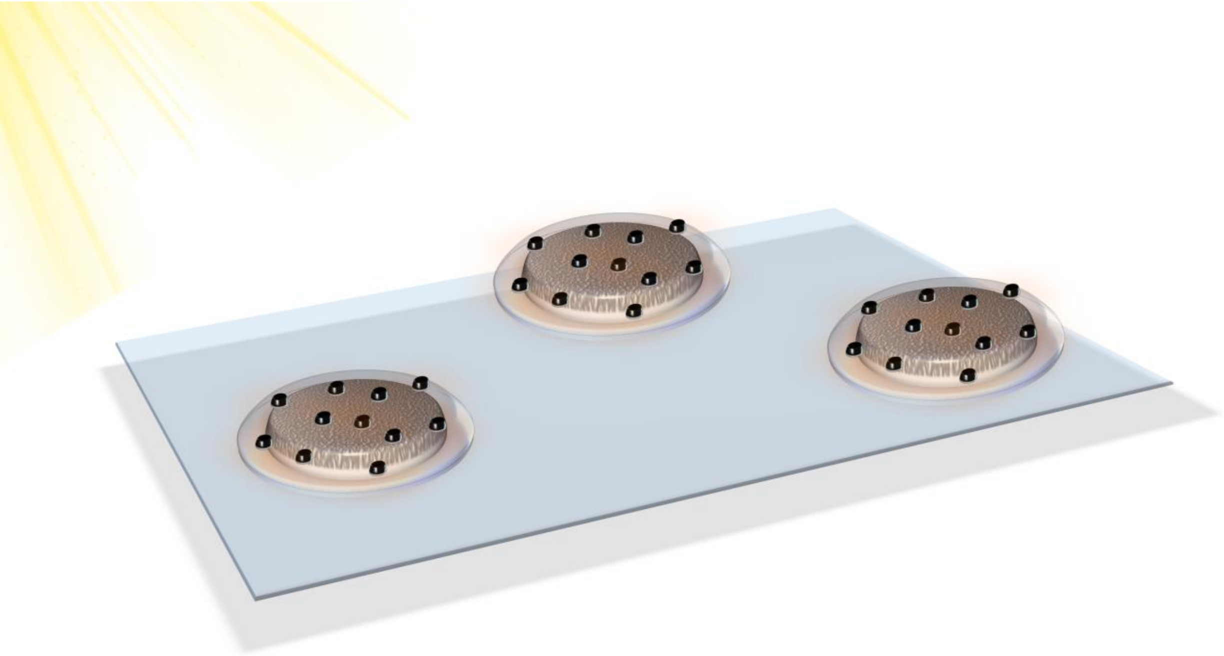

Nanofabrication for Plasmon-Mediated Catalysis via Absorption Engineering

Master Thesis for M.Sc degree in Erasmus Mundus Master Program of
Nanoscience and Nanotechnology

IWAN DARMADI

Department of Physics
CHALMERS UNIVERSITY OF TECHNOLOGY
Gothenburg, Sweden 2016

Education and Culture DG
ERASMUS MUNDUS
KU LEUVEN

Thesis for the degree of Master of Science in Nanoscience and Nanotechnology

Nanofabrication for Plasmon-Mediated Catalysis via Absorption Engineering

IWAN DARMADI

CHALMERS
UNIVERSITY OF TECHNOLOGY

KU LEUVEN

Education and Culture DG

ERASMUS MUNDUS

Department of Physics

Division of Chemical Physics

Chalmers University of Technology

Gothenburg, Sweden 2016

Nanofabrication for Plasmon-Mediated Catalysis via Absorption Engineering

IWAN DARMADI

© IWAN DARMADI, 2016

Supervisor: Svetlana Alekseeva, Department of Physics, Chalmers University of Technology, Sweden

Examiner: Christoph Langhammer, Department of Physics, Chalmers University of Technology, Sweden

Co-promoter: Hiroshi Uji-i, Department of Chemistry, KU Leuven, Belgium

Department of Physics
Division of Chemical Physics
SE-412 96 Gothenburg, Sweden
Telephone +46 31 772 10 00

Cover story: Illustration of dielectric-encapsulated plasmonic silver nanodisks of nanometer size decorated with small platinum nanoparticle catalysts fabricated on a substrate (*not to scale*). The magenta glow surrounding the nanodisk illustrates the light-induced plasmonic-enhanced field absorbed by the adjacent platinum nanoparticle.

Printed by: Chalmers Reproservice
Gothenburg, Sweden 2016

Nanofabrication for Plasmon-Mediated Catalysis via Absorption Engineering

Iwan Darmadi

Department of Physics

Division of Chemical Physics

Chalmers University of Technology

Gothenburg, Sweden 2016

ABSTRACT

The Localized Surface Plasmon Resonance (LSPR) is a unique property of nano-scale materials. It is a resonant response of the electrons of the material to irradiated light at optical frequencies. One of the interesting effects of the resonance is the significant enhancement of the electromagnetic field surrounding the plasmonic nanoparticle. This enhancement can be utilized for a number of applications, one of them is to enhance the light absorption in small catalyst nanoparticles and thus potentially increase the catalytic reaction rate via photocatalytic (hot electron) mechanisms. It is worth noting that catalysts are indispensable to build an eco-friendly society due to their applications in e.g. waste/pollution treatment and emerging sustainable energy technologies. With this spirit, I developed a nanofabrication concept to enable proof-of-concept experiments of light absorption enhancement in Pt catalyst nanoparticles by the LSPR of an adjacent Ag nanoparticle. Interestingly, the LSPR of the Ag nanoparticles occurs in the visible light spectral range, potentially enabling solar energy harvesting to enhance catalytic reaction using the developed nanostructures. In order to demonstrate the enhancement, I developed three different fabrication methods by modifying the so-called hole-mask colloidal lithography (HCL) nanofabrication platform. Specifically, I investigated three methods for the deployment of the sacrificial layer by testing three different materials, namely, PMMA, chromium, and carbon. The hetero-nanostructures fabricated with the PMMA sacrificial layer exhibited absorption enhancement in the

Pt nanoparticles of at least a factor of 8. The expected structure was not successfully attained by the two latter sacrificial layer materials, however. The origins of the failure i.e. the undercut process and the atomic layer deposition are documented and addressed in this report.

Keywords: **nanofabrication, LSPR, catalyst, absorption enhancement, hole-mask colloidal lithography, sacrificial layer**

ACKNOWLEDGEMENTS

Thanks to my examiner Christoph Langhammer for the opportunity to do this challenging project. I am also grateful to be involved in this research group. Thanks for every discussions and the thorough corrections on my written report.

Thanks to my daily supervisor Svetlana Alekseeva for guiding and teaching me since the very beginning till the end of this master thesis project. She contributed a lot in this work.

Thanks to all colleagues in the Langhammer group and Chemical Physics division for their help, friendly chats and *of course*, the *fika*!

Thanks to Chalmers Cleanroom staffs for their help and advice during the nanofabrication.

Thanks to Indonesia Endowment Fund for Education (LPDP-RI) for the financial support of my two-year-study in Belgium and Sweden.

Finally, I thank my family and friends for their moral support.

Iwan Darmadi, Gothenburg, 20 June 2016

TABLE OF CONTENTS

ACRONYMS

LSPR	Localized Surface Plasmon Resonance
SPP	Surface Plasmon Resonance
PVD	Physical Vapor Deposition
CVD	Chemical Vapor Deposition
PECVD	Plasma-Enhanced Chemical Vapor Deposition
ALD	Atomic Layer Deposition
RF	Radio Frequency
PDDA	Poly(diallyldimethylammonium chloride)
PMMA	Poly(methyl methacrylate)
PS	Polystyrene
IPA	Isopropanol
CL	Colloidal Lithography
SCL	Sparse Colloidal Lithography
NSL	Nanosphere Colloidal Lithography
HCL	Hole-mask Colloidal Lithography

CHAPTER 1: INTRODUCTION

1.1 Background

The Localized Surface Plasmon Resonance (LSPR) has been a hot topic of research due to its potential applications [1]–[3]. The LSPR is a resonance of the electrons of a nanoscale material, which is mainly associated with noble metals interacting with light. The resonance leads to many interesting effects that are attractive for applications. For example, a spectral shift of the resonance peak induced by a change of the refractive index of the environment facilitated by the enhancement of the field surrounding the material. The shift and the field enhancement are the basis of nanoplasmonic-based chemical and biological sensors [2], [4], [5]. The other well-known application utilizing the enhanced field is Surface Enhanced Raman Spectroscopy (SERS) [3], [5]. The potential applications of the LSPR are not limited to the ones mentioned above. Another exciting applications are related to plasmon-assisted catalysis [6]–[8], which is the driving force of the present project.

There are at least two approaches to improve catalyst performance by utilizing plasmons: direct hot electron transfer and the absorption enhancement [9]. The former method has been demonstrated with the noble metals e.g. Au and Ag [7], [8], [10]. The noble metals exhibit LSPR in the visible light spectral range and by the fact that the solar spectrum has maxima at the visible range, in principle, we can use this unlimited source of energy to mediate catalytic reactions. The catalytic properties of the traditional plasmonic metals Ag and Au are, however, quite limited. It is the transition metals like Pt, Pd, Ru, Ni, Co, Fe and Rh, which are the most widely used catalysts in industries and environmental cleanup technologies today due to their excellent performance and selectivity. In spite of this excellence, when it comes to plasmon-mediated photocatalysis, the metals above have a disadvantage as they exhibit (very weak) LSPR in the UV range when they are in nanoscale size. Furthermore, the plasmonic quality of the transition metals is relatively low due to their low field enhancements and low resonance factors caused by their large imaginary permittivity in the visible spectral range due to inter- and intraband transitions.

Since the noble metals like Au and Ag exhibit excellent LSPR quality but rather poor catalytic activity (exceptions exist!) and the transition metals like Pt or Pd on the other hand are excellent catalysts but have poor plasmonic properties, there is an idea to combine both of these materials together to obtain the maximum performance in a plasmon-mediated catalysis context. Specifically, it is predicted that optimized plasmon-mediated photocatalytic activity is achievable by exploiting a so-called “absorption engineering” approach [11]–[14]. In this approach, the noble metal plasmonic nanoparticle has a role of the visible light “collector” due to its optimal LSPR performance in the solar spectral range and closely adjacent small transition metal nanoparticles act as the catalytically active sites. The catalyst material is placed in the plasmon-enhanced field of the noble metal to increase the light absorption in the catalyst via near field coupling to the plasmonic nanoparticles. In this way it is predicted to become possible to enhance the rate of electron-hole pair formation in the catalyst by at least one order of magnitude compared to direct light absorption by the small transition metal catalyst nanoparticles [13]. The use of the plasmon-enhanced local fields to improve catalytic reaction has been demonstrated, for example in Ag/TiO_2 [15] and Au/zeolite [16] heterostructures.

This project is motivated especially by the work of Antosiewicz et al. on the absorption engineering in plasmonic and catalyst hetero-nanostructures [11]–[14]. Theoretical calculations by Antosiewicz et al. with the FDTD (finite-difference time-domain) method have shown that hybrid nanostructures comprised of a noble metal nanoantenna (Ag) and closely adjacent catalytic material (Pt nanoparticles) results in significant absorption enhancement as high as 1-2 order of magnitude in the catalyst [13]. Besides the theoretical model, they successfully fabricated the plasmonic-catalytic hetero-metallic nanostructure with hole-mask colloidal lithography (HCL) [17] and confirmed that the absorption is enhanced by at least 1 order of magnitude. However, the samples used in that study have a shortcoming in that the catalyst particles were located not only in LSPR enhanced-field zone, i.e. also in the area between plasmonic antennas (which only have a ca. 10% surface coverage). Consequently, the measured absorption comes from both the catalyst which is in the influence zone of the LSPR and those which are not under influence of the LSPR. Therefore, it is not clear how the LSPR of the nanoantenna affects the catalyst absorption. Motivated by this shortcoming, we conducted this project to develop a method to fabricate nanostructures surfaces where the catalyst nanoparticles *exclusively* are localized in the LSPR enhanced-field zone - as illustrated in this report's cover page - in order to get more accurate insight in the absorption enhancement.

In this project, I focus on the nanofabrication method development of hetero-metallic nanostructures comprised of Ag nanoantennas covered by a thin dielectric spacer layer and Pt nanoparticles that are distributed only inside the influence zone of the LSPR (of Ag). Silver is chosen for the plasmonic antennas because of its low plasmonic loss [18]. The dielectric spacer - which is either oxide or nitride thin film - is a crucial part of the nanostructure as it encases the Ag, which otherwise is prone to oxidation. Moreover, the spacer has the function to draw and concentrate the enhanced-field away from the substrate. The fabrication method that I used and optimized is the hole-mask colloidal lithography (HCL) method - a sub-variant of colloidal lithography (CL) [17]. The spacer layer deposition is the central challenge in the fabrication since the deposition has to be performed while the Ag nanoantenna is still located inside a nano-sized well defined by the mask used for the nanofabrication. The aim is to achieve a dielectric layer of good uniformity and conformality which, as it turns out, is not straightforward to achieve since the deposition precursors experience more impediment to penetrate to the narrow well. Furthermore, since the spacer deposition is executed in the presence of the mask and the sacrificial layer, one has to consider the compatibility of the mask and sacrificial layer materials with the spacer deposition process (e.g. substrate temperature up to 300 °C).

The short-term aim of the project is to fabricate the aforementioned hetero-nanostructures, which will provide a better way to investigate the correlation of the LSPR and the absorption enhancement in an adjacent transition metal nanocatalyst. For long-term goal, we also expect that the development of the fabrication method will be useful for other nano-plasmonic applications e.g. nano-plasmonic sensing and spectroscopy.

1.2 Purpose

The purpose of this project is to optimize nanofabrication of plasmonic-catalytic metallic hetero-nanostructures and to gain deeper understanding of how the LSPR influences the absorption enhancement of an adjacent transition metal catalyst material.

1.3 Objectives

This study has several objectives such as:

1. Fabrication and characterization of Ag and Pt nanostructures with the HCL method. Three kinds of samples were fabricated on the silicon/borosilicate glass substrate: (i) dielectric-encased Ag nanodisks, (ii) Pt nanoparticles on the dielectric thin film (iii) the complete structure of Ag/dielectric spacer/Pt. To achieve this, three methods differing in the sacrificial layer materials, namely, chromium, carbon, and PMMA, were used.

2. Measurement of the light absorption of the nanostructure under ultraviolet and visible light irradiation. Later, the measurement results of the aforementioned

samples (i), (ii), (iii) will be compared to see how the LSPR influences the absorption of the nanostructure.

CHAPTER 2: PLASMONICS AND ABSORPTION ENGINEERING

2.1 Plasmons

In metals, the valence electrons are relatively “free” compared to their counterparts semiconductors or insulators. Understanding the valence electron response to external perturbation is very important to evaluate the physical properties like e.g. heat transport, electrical transport, and optical properties. Later in this chapter, the valence electrons will be called electrons only for simplification reason.

The electrons in metals can be regarded as ideal gas within the so-called Drude model [19]. The model explains how the electrons behave in the presence of an electromagnetic wave. The dynamics of one electron is then,

$$m_e \frac{\partial^2 \boldsymbol{r}(t)}{\partial t^2} + m_e \Gamma \frac{\boldsymbol{r}(t)}{\partial t} = -e\boldsymbol{E}(t) \qquad \textit{eq. 1}$$

With the m_e and e as the effective mass and the charge of the electron, respectively. The displacement of the electron is denoted as $\boldsymbol{r}$, under external field influence $\boldsymbol{E}$**.** The first term is simply Newton’s second law while the second term arises due to the fact that the electron is damped by its surrounding environment. The Γ coefficient tells us the strength of the damping.

By solving the eq. 1, the displacement of the electron in the frequency domain can be expressed as:

$$\boldsymbol{r}(\omega) = \frac{e}{m_e(\omega^2 + i\Gamma\omega)}\,\boldsymbol{E}(\omega) \qquad \text{eq. 2}$$

In the bulk, a number of electrons are displaced to form a collective (macroscopic) polarization:

$$\boldsymbol{P} = -ne\boldsymbol{r} = \frac{-ne^2}{m_e(\omega^2+i\Gamma\omega)}\,\boldsymbol{E} \qquad \text{eq. 3}$$

Where n is the electron density in the bulk.

From different perspective, the polarization that is built up in a material can also be defined as:

$$\boldsymbol{P} = \varepsilon(\varepsilon_0 - 1)\,\boldsymbol{E} \qquad \text{eq. 4}$$

By comparing eq. 3 and eq. 4, the permittivity of the material is then,

$$\varepsilon(\omega) = 1 - \frac{ne^2}{\varepsilon_0 m_e(\omega^2 + i\Gamma\omega)} = 1 - \frac{\omega_p^2}{(\omega^2 + i\Gamma\omega)} \qquad \text{eq. 5}$$

The permittivity (ε) reflects the susceptibility of the material to build polarization under the influence of an external field. When the frequency of the external field equals the so-called plasma frequency (ω_p), the electron “gas” is collectively excited in a so-called plasmon. Above this frequency, the electromagnetic wave is transmitted because the electrons cannot follow it. On the other hand, the electromagnetic wave of lower frequency is reflected. For example, the plasma frequency of Ag occurs at around 9.5 eV (or equivalent to wavelength of 130 nm). Therefore, silver looks shiny because it reflects all visible frequencies. It is worth noting that although we focus the discussion on the plasmonic phenomenon in metals, plasmonic materials are not limited to metals, other novel plasmonic materials like nitride and silicon-based doped semiconductors have also been reported. However, the performance is inferior to the “traditional” plasmonic metals [18].

2.2 Plasmons in Nanoscale Metals

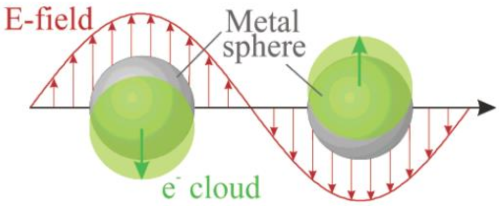

Figure 1 Localized surface plasmon resonance. The free electrons of a nano-sized metal oscillate coherently, driven by the electric field of an irradiated electromagnetic wave (adapted from [20]).

The plasma oscillation in a nanoscale material (the dimension is much smaller than the light wavelength), behaves differently from the plasmon in the bulk or the surface of a metal. Along the metal’s surface the plasmon propagates to form a so-called surface plasmon polariton (SPP). For simplicity SPP can be called as surface plasmon. However, when the dimension of the metal is much smaller than the wavelength, the surface plasmon does not propagate any longer, but forms a localized surface plasmon resonance (LSPR) (Figure 1).

LSPR is a very interesting nanoscale property of a metal because the field around the surface of the nanoparticle is enhanced significantly, as a consequence of the charge polarization. This enhancement can be exploited for a number of applications e.g. absorption engineering of catalysts as in focus in this project.

The earliest work that describes the interaction of very small particles ($d \ll \lambda$) with light was published by Gustav Mie. By solving Maxwell’s equations, he could show the absorption and scattering behavior of a small-sized sphere. The absorption and the scattering cross-sections can be expressed as (after dipole approximation, the paper by Mayer and Hafner [2] is a good reference to see the simple derivation):

$$\sigma_{ext} = \frac{18\pi\varepsilon_m^{3/2}V}{\lambda}\frac{\varepsilon_2(\lambda)}{[\varepsilon_1(\lambda)+2\varepsilon_m]^2+\varepsilon_2(\lambda)^2} \qquad \textit{eq. 6}$$

$$\sigma_{sca} = \frac{32\pi^4\varepsilon_m^2V^2}{\lambda^4}\frac{(\varepsilon_1-\varepsilon_m)^2+(\varepsilon_2)^2}{[\varepsilon_1(\lambda)+2\varepsilon_m]^2+\varepsilon_2(\lambda)^2} \qquad \textit{eq. 7}$$

$$\sigma_{abs} = \sigma_{ext} - \sigma_{sca} \qquad \textit{eq. 8}$$

From the equations above, the absorption of the small nanoparticle is highly dependent on the dimension (V) and the surrounding medium (ε_m). The real part and the imaginary part of the metal dielectric function are denoted by the symbol ε_1 and ε_2, respectively. For a nanoscale object, the absorption cross-section can be larger than its geometrical cross-section [21].

The absorption and scattering by the nanoparticle are actually the consequences of the plasmon oscillation decay. The dissipated energy bifurcates into two processes: re-emitting a photon (radiative process) or creation of electron-hole pair (non-radiative process). The former is associated with scattering while the latter with absorption. The dimensions of the nanoparticle determine which process is more dominant than the other. For instance, Ag nanoparticles for the size larger than 50 nm they predominantly scatter while particles smaller than 30 nm predominantly absorb light [6].

2.3 Using Plasmons to Enhance Catalytic Reactions

There are at least two main ways of utilizing plasmons to enhance catalytic reactions. First, direct transfer of hot electrons which are induced by plasmon decay, to the reactants. Secondly, using the enhanced field induced by the plasmon.

In the first method, the plasmon excitation induces the creation of hot electrons at the surface of the metal. One can harvest this plasmon enhancement efficiently from nanoparticles in which absorption is the dominant plasmon decay process. There are several reports that demonstrated plasmonic nanoparticle such as Ag and Au can dissociate adsorbed molecules in the presence of light [7], [8]. For example, Christopher et al. demonstrated that Ag nanocubes ~ 60 nm performed enhanced catalytic reaction at the plasmon resonance [7]. The nanocube successfully assisted epoxidation of ethylene, oxidation of carbon monoxide and oxidation of ammonia. The proposed mechanism was that the hot electron drives the adsorbed O_2 molecules in to transient negatively charged state (O_2^-). Later, the O_2 dissociates because the energy of this transient state is higher than the dissociation activation energy (E_a). Finally, the dissociated oxygen oxidized the reactants.

As the plasmon resonance of Ag and Au occurs at visible light photon energies, the first method is very advantageous in the sense of solar energy harvesting. However, this method has an issue with selectivity because in principle the hot electron can drive dissociation of any molecules that are present, provided their energy matches the unoccupied molecular orbitals of an adsorbate.

The second method of enhancement involves the scattering (radiative) process. The electric field at the surface of the nanoparticle is enhanced significantly compared with the intensity of the incident light. The field at the surface can be enhanced by 3 orders or even 6 orders of magnitude in certain nanoparticle arrangements [6]. Maximum enhancement occurs right on the surface and decays exponentially away from the surface. The zone of the enhancement is of the order of tens of nanometers. It is worth noting that the zone depends on the shape of the material [20].

The main idea of this method is to put small (few nm) nanoparticles of a catalyst material in the zone of enhanced plasmonic field from a larger plasmonic structure (tens of nm) to increase the absorption of light in the catalyst via the field concentration. In the following process, the enhanced field thus excites the electrons of the catalyst that are useful for catalytic process more efficiently as direct photo-excitation of the catalyst itself. In this way, the nanoparticle acts as field concentrator for the catalyst particle. One example of the realization of this method is reported by Kumar et al. [15]. They fabricated Ag/SiO_2/TiO_2 nanostructures where the Ag acts as plasmonic field concentrator, the TiO_2 as the catalyst material and the SiO_2 as the spacer in between those two. The SiO_2 spacer of 2 nm is thin enough to allow the TiO_2 to sit within the plasmonic enhanced field. To demonstrate the role of the plasmonic-enhanced field, they compared the degradation rate of methylene blue (MB) catalyzed by TiO_2 only to the degradation rate by plasmon-assisted TiO_2. They observed a significant rate enhancement by the TiO_2 in the presence of the Ag nanoparticle.

CHAPTER 3: THE NANOFABRICATION AND THE CHARACTERIZATION TECHNIQUES

3.1 Spin Coating

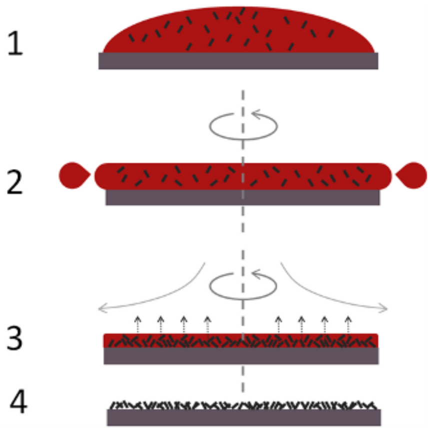

Figure 2 The spin coating process for thin film deposition (adapted from http://www.ossila.com/pages/spin-coating).

One of the most efficient ways to deposit polymer thin films is by spin coating. The principle of this coating technique can be summaries as follows. (1) The solution of polymer is dropped on to the substrate. (2) The spinner is accelerated to certain angular speed and consequently, the centrifugal force spreads the solution from the center towards the edge of the substrate. (3-4) The airflow, which is part of the spinner system, assists evaporation of the solvent, leaving a thin film of polymer on the substrate.

The obtained thickness of the thin film depends on both the polymer solution itself (e.g. concentration, drying rate, surface tension) and the spinner system (e.g. speed, time, acceleration, exhaust, humidity). In general, the more speed and time, the thinner the thin film. The thickness (t) relation with the angular speed (ω) can be expressed as,

$$t \propto \frac{1}{\sqrt{\omega}}$$

In this project, spin coating technique is employed to deposit PMMA (*Poly(methyl methacrylate*) of thickness 40 nm. We used the most diluted PMMA available in the cleanroom, that is PMMA A2 provided by MicroChem. The thinnest thin film we can achieve was ca. 50 nm by $7000 - 8000$ rpm angular speed (8000 rpm is the maximum speed available in the MC2 cleanroom spinner system). The thinner film is later achieved by using O_2 plasma to reduce the thickness.

3.2 Electron Beam Physical Vapor Deposition (E-Beam PVD)

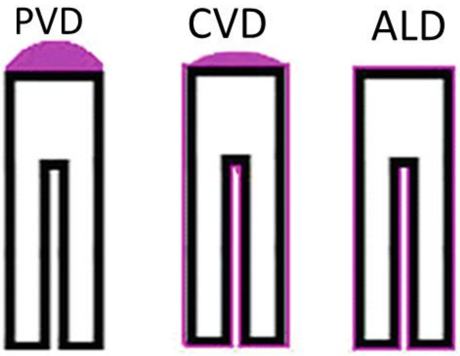

Figure 3 Conformality comparison of thin films grown by PVD, CVD and ALD (adapted from [22]).

The basic principle of PVD is evaporation of a source material and transporting the vapor to the sample surface followed by vapor condensation on the surface. PVD can be employed to deposit both metals and oxides. The advantages of PVD are the high deposition rate (up to 1µm/s), high purity of the thin films due to high vacuum environment, and scalability to large wafers. The PVD has shadowing and low conformity effects in comparison to CVD (Figure 3).

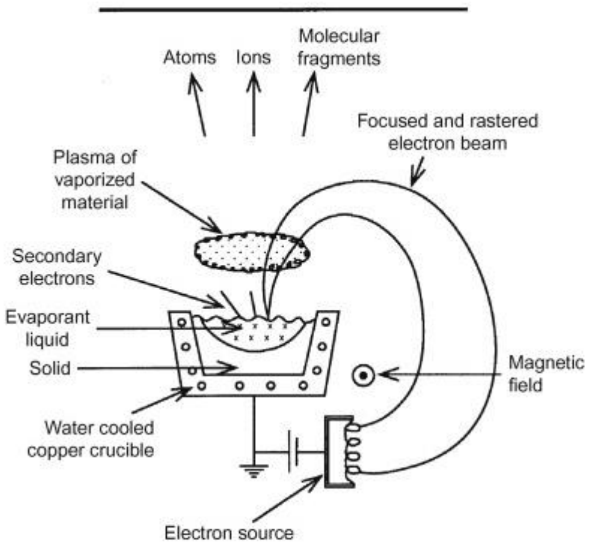

Figure 4 The schematic of electron beam-PVD (adapted from [23]).

In this nanofabrication project, an electron beam PVD is employed. The evaporation with this type of PVD is achieved by the heating created when a high-energy electron beam hits the target material/source. The source of the electron is a high voltage cathode filament (in order of some kilo volt). The electron beam is then guided in circular way to the material source by a magnetic field (Figure 4). In order to obtain high purity of deposited material, good vacuum conditions on the order of 10^{-6} Torr has to be fulfilled. Today, as the pumping technology is more developed, deposition of high purity materials is not a big issue anymore.

3.3 Plasma Enhanced Chemical Vapor Deposition (PECVD)

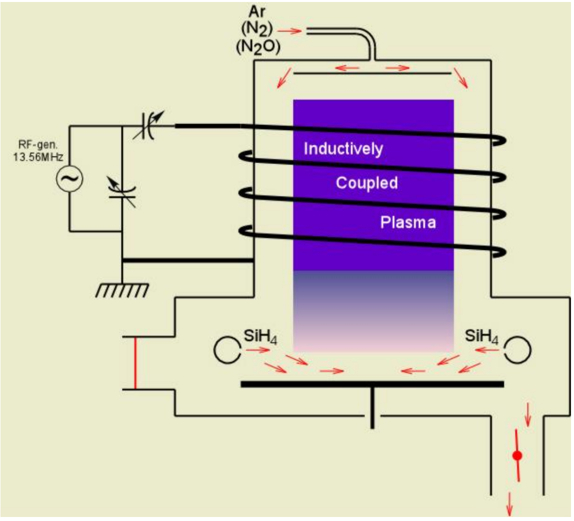

Figure 5 The schematic of the plasma enhanced chemical vapor deposition (PECVD) (source: Tool 404 tutorial by Mats Hagberg, Chalmers).

The chemical vapor deposition (CVD) is a type of deposition that employs volatile compounds to react with each other to form a desired thin film on the solid substrate. The CVD coats any surface that is exposed to the precursors, compared with PVD that coats only the surface facing towards the material source (Figure 3). The schematic of the CVD process involves an oven to assist the reactions. The heating is the key in CVD. For instance, oven temperature of $650\ ℃$ is required to deposit Si from gaseous SiH_4 by pyrolysis process [24].

The deposition of silicon nitride (Si_3N_4), the material of interest in this project, requires oven temperature of $750\ ℃$ in normal CVD operation,

$$3SiCl_2H_{2(g)} + 4NH_{3(g)} \rightarrow Si_3N_{4(s)} + 6H_{2(g)} + 6HCl_{(g)}$$

The oven temperature as low as $300\ ℃$ is possible with SiH_4 and NH_3 precursors but the deposited thin film will contain more hydrogen [24].

There are some variants of the CVD, namely APCVD (atmospheric pressure CVD), LPCVD (low pressure), LECVD (laser enhanced), and PEVCD (plasma enhanced). The latter variant is of our interest in this project due to its low temperature operation (room temperature).

The schematic of the PECVD process by Oxford Plasmalab System 100 is illustrated in Figure 5. The precursor gases, namely, Ar and N_2, are fed from the top of the chamber. The winding coil connected to the RF generator creates an Ar and N_2 plasma that subsequently reacts with the SiH_4 gas that flows on the substrate. As the deposited silicon nitride is non-stoichiometric, it is denoted by the formula SiN_x. The thin film growth rate is $144\ \text{Å}/min$ and the refractive index at λ_{633nm} is 1.99.

3.4 Atomic Layer Deposition (ALD)

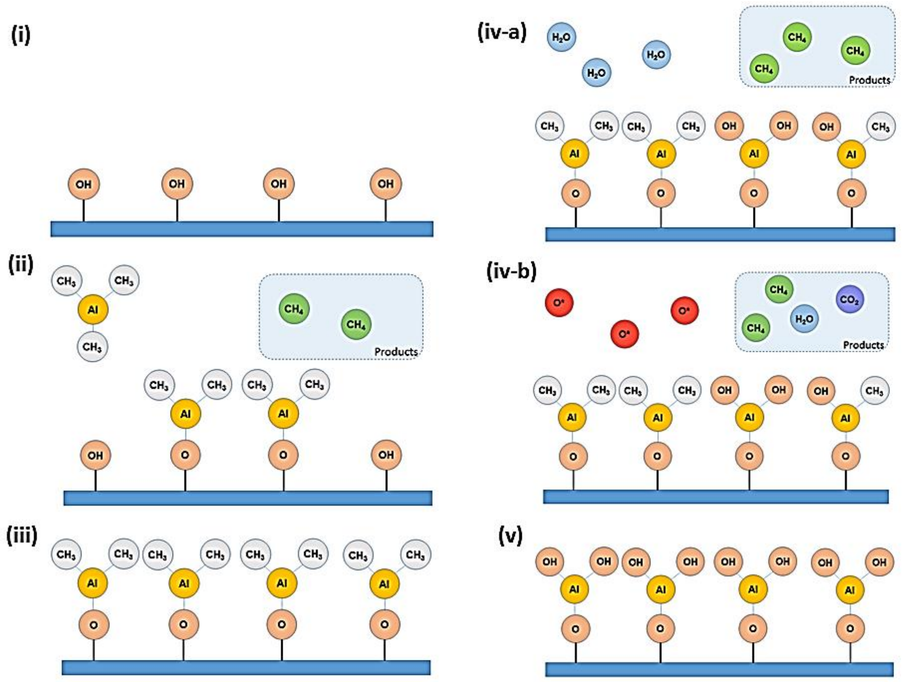

Figure 6 Mechanism of the atomic layer deposition (ALD).

The atomic layer deposition (ALD) is a thin film deposition technique based on sequential reactions of gases on a surface to form thin layer of a solid. The ALD has a high reputation of high quality and thickness precision of the thin films created and it is mostly employed for oxide deposition. The aluminum oxide (Al_2O_3), the material we used as a spacer in this project, is a good model to explain how the ALD works[25].

There are two types of ALD based on the oxidization process: thermal and plasma enhanced ALD. The former process is explained as follows (Figure 6). (i) The process begins by substrate functionalization with hydroxyl groups (-OH) to assist the following chemisorption. (ii) Later, the functionalized surface is exposed to the first precursor TMA (*trimethylaluminium*). The TMA reacts with the hydroxyl leading to *dimethylaluminium-oxide* and CH_4 as the product. (iii) The reaction stops when the entire surface is completely covered with *dimethylaluminium-oxide*. The excessive TMA and methane product is then purged out. (iv-a) The second precursor water (H_2O) oxidizes the *dimethylaluminium* resulting in methane as reaction product. In this process, the reaction is assisted by thermal energy, thus it is named as thermal ALD process. (v) The excessive water and methane product are purged out and then it is ready for the next cycle of TMA and water exposures.

The plasma enhanced ALD process is similar to the thermal process except that it deploys oxygen plasma radicals instead of water to oxidize the *dimethylalumnium* (iv-b). While the thermal process requires high temperature condition, the plasma process can take place at lower temperatures.

3.5 Etching

Etching is a process of removing the unwanted part of a material in nanofabrication. There are two kinds of etching processes: wet and dry process. The wet etching process employs liquid phase chemicals whereas the dry process employs gas phase species or plasma as the etchant. The former process removes material by chemicals reaction while the latter by both chemical reaction and mechanical energy.

The wet etching is a relatively low cost process because it can be done at ambient conditions. However, the liquid chemical as the reactants and the products is more difficult to handle. On the other hand, the dry etching requires higher cost since it has to be done in vacuum condition.

The wet etchant in general consists of three ingredients: the oxidizer, acid or base as the oxide dissolvent, and the dilutant. The removing process is initiated by the oxidation of the unwanted material by a strong oxidizer, such as H_2O_2 or HNO_3. Subsequently, the oxide is dissolved by acid or base. The dilutant, for example water, plays important role to transport the reactants (products) onto (from) the surface of the undesired material.

In this nanofabrication project, the etchant is expected to etch material through a nanoscale hole. As mentioned before, the transport of the reactants (products) onto (from) the etch target is very crucial to achieve successful removal. Thus, it is also very important to mention *hydraulic resistance* (R_h) to understand how the diameter and the length of the channel determine the success of the process. The *hydraulic resistance* tells how easy a fluid flows through a channel. It depends on the shape, the length (L), and the radius (r) of the channel and the viscosity (η) of the fluid. For a channel with circular cross section, the *hydraulic resistance* is [26]:

$$R_{hyd} = \frac{8}{\pi}\eta L \frac{1}{r^4} \qquad \textit{eq. 9}$$

From the equation above, one can see that the fluid experiences more resistance by the power of four as the channel radius is reduced.

(A) Chromium Wet Etching

In this project, Chromium is deployed as a sacrificial layer. The wet etchant is used for two purposes: to make an undercut and to perform lift off. The Chromium etchant is a mixture of ceric ammonium nitrate, acid, and water. The chromium etching reaction is then [27]:

$$3Ce(NH_4)_2(NO_3)_{6(aq)} + Cr_{(s)} \rightarrow\ Cr(NO_3)_{3(aq)} + 3Ce(NH_4)_2(NO_3)_{5(aq)}$$

The products of the reaction are soluble. The acid acts as the ceric ammonium nitrate stabilizer.

The chromium etchant in this fabrication used the etchant provided by SunChem AB. The composition of the etchant is $10-15\%$ ceric ammonium nitrate, $0-10\%$ glacial acetic acid, $0-10\%$ nitric acid, and $70-80\%$ water.

(B) Oxygen Plasma Dry Etching

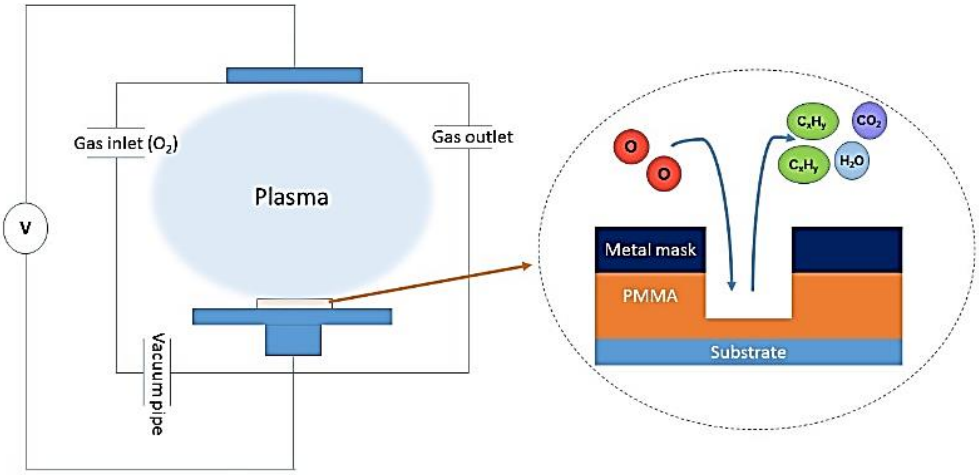

Figure 7 Schematic depiction of the oxygen plasma etching set up (left). The oxygen radicals etch the polymer and form volatile products (right).

Plasma is one of the four states of matter in the universe. The plasma is a state with equal number of unbounded positive and negative charges, thus overall it is neutral. One way to create plasma is by applying high electric fields to the gases between two electrodes in order to ionize the molecules. In this project, we used oxygen plasma to etch PMMA or a carbon thin film to make the nanoholes in the metal mask fabricated by Hole-Mask Colloidal Lithography (HCL).

The oxygen plasma etching process is illustrated in Figure 7. The oxygen is supplied through the gas inlet to the high vacuum chamber. The high voltage difference between the electrodes separates the formed oxygen ion, O^+, and an electron. The created high kinetic energy electron then collides with other O_2 molecules. There are two products of this collision, oxygen ionization:

$$O_2 + e^- \rightarrow O^+ + 2e^-$$

and oxygen radicalization:

$$O_2 + e^- \rightarrow 2O + e^-$$

The oxygen radical, which is much more abundant than the oxygen ion, is responsible for the polymer etching. It chemically etches the polymer by forming volatile products such as water, carbon dioxide, and carbon hydroxyl group.

3.6 Scanning Electron Microscope (SEM)

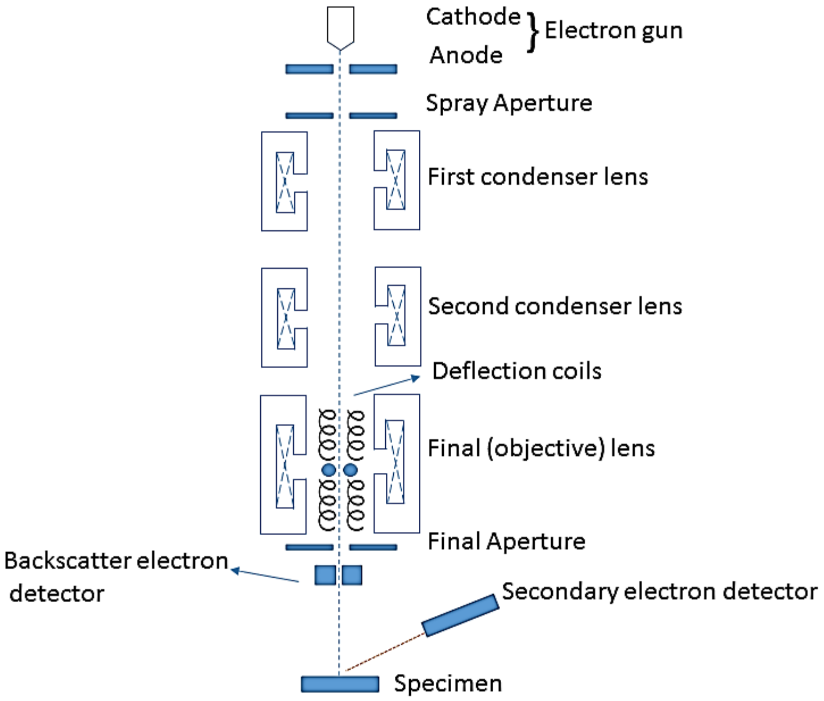

Figure 8 Schematic of scanning electron microscope (SEM) (adapted and simplified from [28]).

Scanning electron microscopy (SEM) is a microscopy based on electrons. The resolution of the microscopy is down to tens of nanometers. A schematic depiction of a SEM instrument is presented in Figure 8. The electrons emitted by a filament (as cathode) are accelerated towards the anode by a voltage difference of several kilo volts. In the next stage, the electrons are condensed by two or more electron condenser lenses. The closest lens to the specimen is the final (objective) lens. The purpose of the objective lens is to move the electron beam such that it hits the specimen with the smallest possible cross-section to gain the best focus.

The deflection coil that is usually located in the inner part of the objective lens has the function to direct the beam on the specimen surface for scanning. Finally, the scattered electrons are collected by the detectors. The first detector close to the objective lens collects the backscattered electron while the other detector collects the secondary scattered electrons.

The SEM employed in this project is Supra 60 VP by Zeiss. Working distance of 4 mm and electron gun voltage of 10-15 kV were used to gain good image of feature sizes on the order of ca. 60 nm.

3.4 Ellipsometry

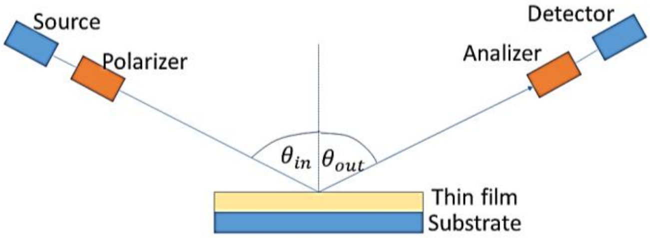

Figure 9 The schematic of a thin film thickness measurement by ellipsometry.

Thin thickness of thin films can be determined by ellipsometry (J.A. Woollam M2000) since any material has a unique response when reflecting a polarized electromagnetic wave. Ellipsometry exploits this property to extract useful information about the material e.g. film thickness or refractive index.

A material reflects an electric field parallel ($\widetilde{r_p}$) and perpendicular ($\widetilde{r_s}$) to the plane of incidence differently. Ellipsometry measures the ratio of those two reflections:

$$\frac{\widetilde{r_p}}{\widetilde{r_s}} = \frac{\tilde{E}_p^{out}/\tilde{E}_p^{in}}{\tilde{E}_s^{out}/\tilde{E}_s^{in}} = \frac{\left|E_p^{out}\right|/\left|E_p^{in}\right|}{\left|E_s^{out}\right|/\left|E_s^{in}\right|} e^{i(\delta_p-\delta_s)} = \tan(\Psi)\, e^{i\Delta} \qquad \text{eq. 10}$$

On the other hand, the reflections of a thin film on a substrate depends on the thickness of the materials [29]. Thus, in principle, by measuring the ratio of the field intensity (Ψ) and the phase difference (Δ), the thickness of the thin film can be extracted.

Ellipsometry in this project was specifically used to measure the thickness of the PMMA sacrificial layer used nanofabrication in a thickness range of $30 - 50\, nm$. As the PMMA is very thin and transparent, the Cauchy model (featured in the ellipsometry software) is deployed to obtain the thickness value.

3.5 Insplorion X1 Flow Reactor

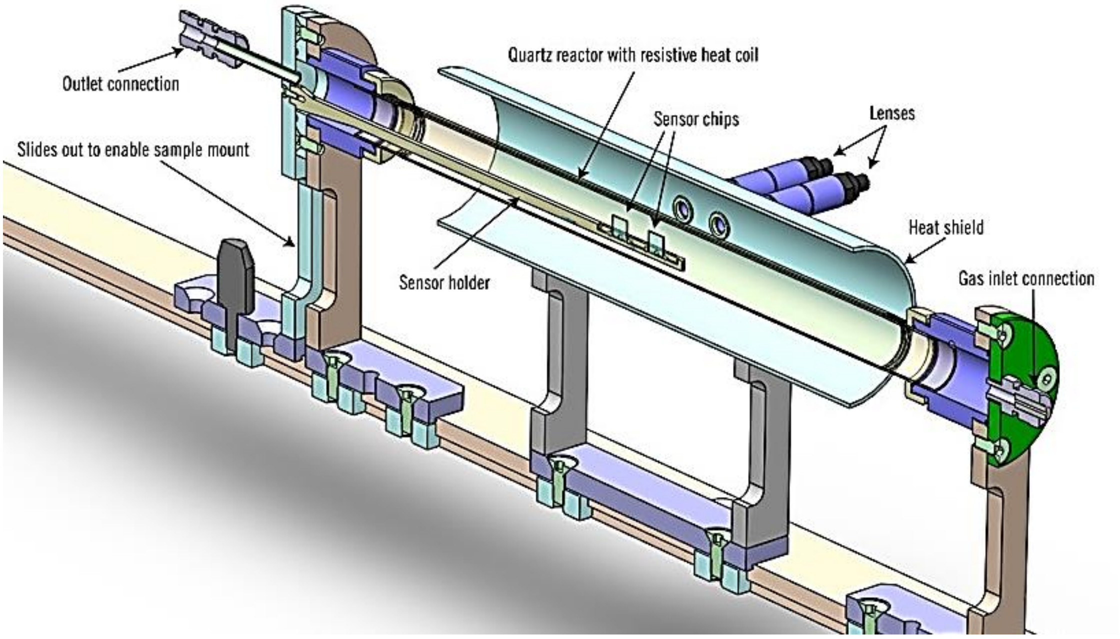

Figure 10 The Insplorion X1 flow reactor set up (image source: Insplorion AB).

The Insplorion X1 reactor was used to test silver oxidation of our samples at high temperatures. A heater coil is wound around the quartz tube. The heater temperature is controlled by DC power supply via a Eurotherm-controlled feedback loop.

The input gas was a mixture of 2% O_2+H_2 and 98% Ar (with total flow $190\ mL/min$). The setup is equipped with UV-spectroscopy to monitor the LSPR extinction in situ. The completely oxidized Ag will lose its extinction peak.

3.6 UV-Visible Spectrophotometer

The UV-visible spectrophotometer (Cary 5000) was employed to measure the extinction and absorption spectra of the fabricated nanostructure within the range of $400 - 1000$ nm. For the purpose of the measurement, the samples were prepared on borofloat (BFG) substrate. The extinction and absorption measurement were collected with different set up.

To measure the extinction, the sample was placed in between light source and the detector. Later, the light transmission (T) was measured and the extinction was extracted (E):

$$E = 1 - T$$

The absorption spectra was measured in a so-called integrating sphere set up. The absorption (A) and extinction intensity relate as:

$$E = A + S$$

Where the S is the symbol denoted for the scattering intensity.

CHAPTER 4: NANOFABRICATION

The deployed method in this project is based on colloidal lithography (CL)[17], [30]–[32]. Colloidal lithography is a way to pattern a structure with colloidal nanoparticles as the mask, thus the fabrication cost is much lower than the conventional lithography where the mask is fabricated with more sophisticated processes such as in electron beam lithography, were an electron beam is used.

The earliest variants of colloidal lithography are nanosphere colloidal lithography (NSL) and sparse colloidal lithography (SCL). In the NSL, the close-packed colloidal nanospheres are deposited on the substrate while in the SCL the colloidal nanospheres are deposited sparsely. In combination with the thin film deposition, the nanostructures of various shapes e.g. crescents, nanocones, and nanodisks can be patterned. There is another variant of CL called hole mask colloidal lithography (HCL) developed by Fredriksson, et al. [17]. The HCL introduces a sacrificial layer to the fabrication process that circumvents most limitations of the NSL and SCL methods, including the need for a reactive ion etch after nanostructure deposition.

In this project, we modified the standard HCL to achieve the desired nanostructures described in the introduction. We used three different approaches differing in the sacrificial layer materials: (i) PMMA, (ii) chromium, and (iii) carbon. As chromium and carbon are thermally stable materials at temperatures as high as $300\ ^{\circ}\mathrm{C}$, the spacer deposition with ALD technique is possible using these materials as sacrificial layers. This is an advantage because ALD theoretically provides better oxide thin film quality and better step coverage than the CVD process. However, the use of these sacrificial layers has a drawback as it for example makes wet etching necessary as part of the processing when chromium is used as sacrificial layer.

On the other hand, the use of PMMA as the sacrificial layer avoids the deployment of wet etching, which is advantageous. However, the deposition of the oxide has to be done with another low temperature technique such as PECVD. PECVD theoretically deposits lower quality and less controllable thin films compared to ALD.

Polystyrene (PS) nanobeads and *Poly(diallyldimethylammonium chloride* (PDDA) are two indispensable parts of colloidal lithography. In the fabrication, we used a negatively-charged PS nanobeads solution provided by Life Technology. Due to their negative surface charge in aqueous solution, the nanobeads repel each other and distribute sparsely on substrate which is positively charged. PS solutions of different average diameters were used: $41nm$, $51nm$, and $58\ nm$ in order to make nanostructures with different sizes (the nanobead size defines the size of the obtained nanostructures at the end of the fabrication). The PS was diluted with water to a concentration of $0.025\ \%$volume. The PDDA is a positively-charged polyelectrolyte solution that has a function form a positively charged monolayer on the surface of the substrate, which will electrostatically attract the negatively charged PS nanobeads towards the substrate. Here, the PDDA used was provided by Sigma Aldrich. It was diluted with water to obtain 0.2%volume concentration.

4.1 Method I: PMMA Sacrificial Layer

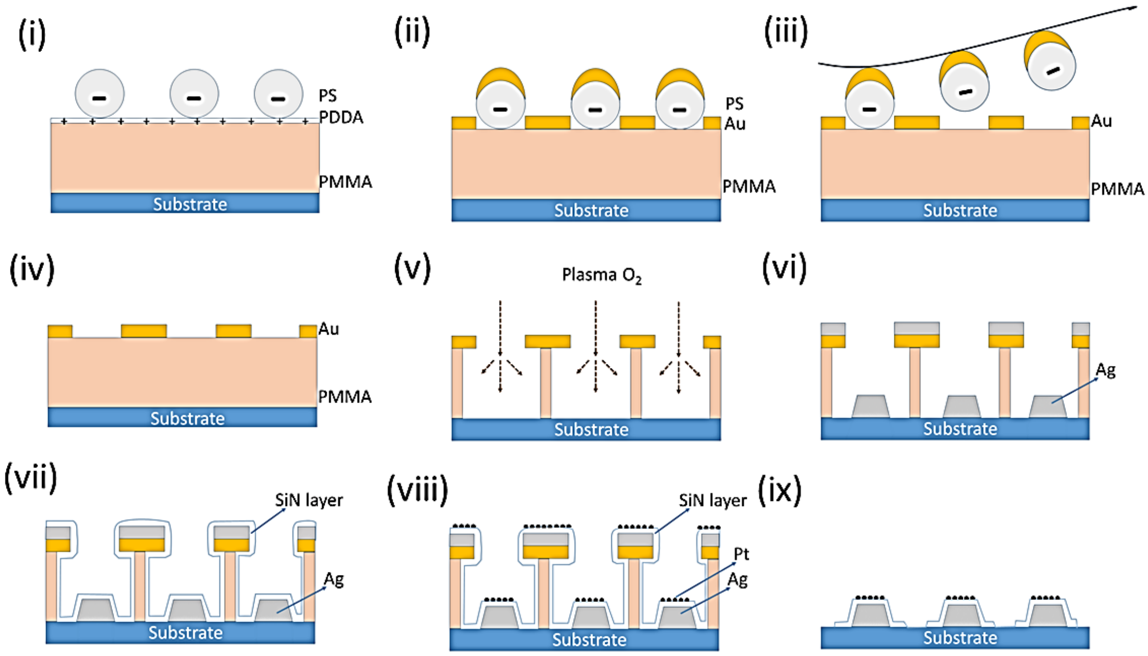

Figure 11 Method I: Fabrication based on PMMA as the sacrificial layer.

The processing steps of the method I are illustrated in Figure 11. Prior to the nanofabrication process, the substrate (either Si or borofloat glass (BFG)) was cleaned with solvents: acetone, isopropanol, and methanol, two minutes each in an ultrasonicator. Later, it was washed in isopropanol, followed by N_2 blow dry. The fabrication process is explained as follows. (i) The PMMA layer was deposited by spin coating $(\omega = 7500\, rpm, \alpha = 2000\, rpm/min)$ for 60 seconds to reach a thickness of approximately 50 nm. Subsequently, it was baked on a hot plate at 170 ℃ for 5 minutes to evaporate residual solvent. Afterwards, it was exposed to O_2 plasma (pressure $50\, mTorr$, RF power $250\, W$, and oxygen flow $10\, sccm$) for 5 seconds. This ashing served two purposes: to reduce the thickness of the PMMA and to reduce its hydrophobicity. The final thickness of the PMMA was approximately 40 nm, confirmed by ellipsometry measurement. The positively charged polyelectrolyte (PDDA) layer was then deposited by drop coating on the PMMA and incubated for 40 seconds, followed by a 10 second wash with flowing water and N_2 blow dry. Subsequently, the PS solution was deposited by drop coating and incubated for 2 minutes, followed by 10 second wash with flowing water and N_2 blow dry. (ii) The gold thin film mask of 15 nm thickness was deposited by e-beam PVD followed by tape stripping to remove the PS, leaving Au thin film with holes as a mask (iii-iv). (v) The exposed PMMA was removed by the O_2 plasma dry etching to make an undercut under the Au mask. The undercut was carefully controlled by adjusting the etching time. (vi) Afterwards, the Ag of 20 nm thickness was deposited by e-beam PVD. (vii) The silicon nitride was deposited by PECVD. (viii) The final deposition was Pt of 5 Å thickness by e-beam PVD. (ix) Finally, the sacrificial layer and the mask were lifted off by ultrasonication in acetone, leaving the final structure on the surface.

4.2 Method II: Chromium Sacrificial Layer

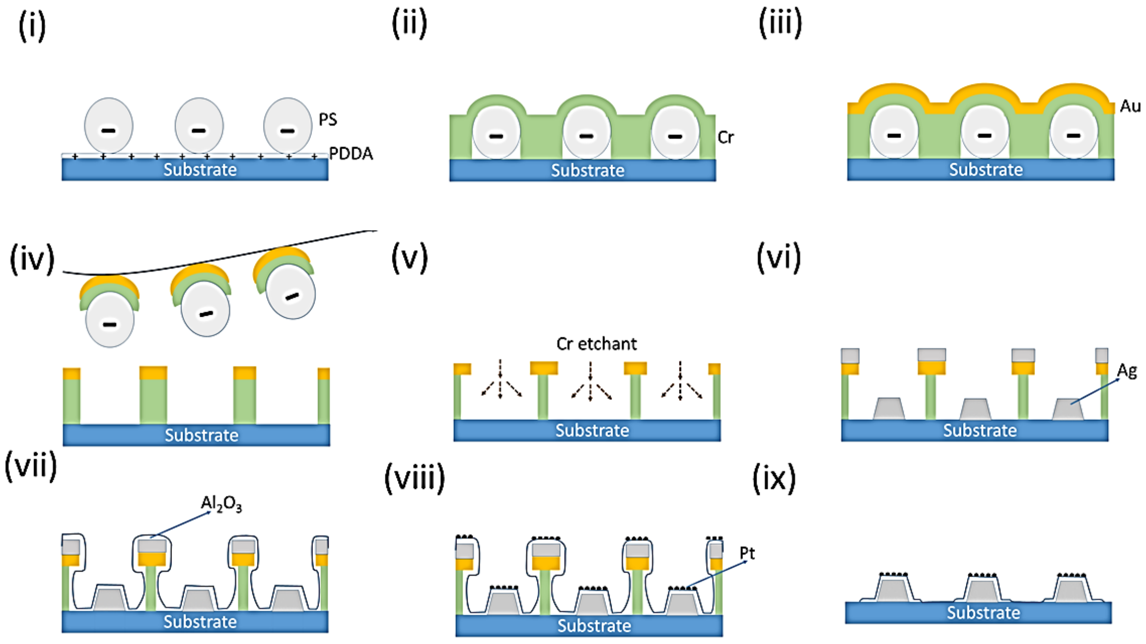

Figure 12 Method II: Fabrication based on Cr as the sacrificial layer.

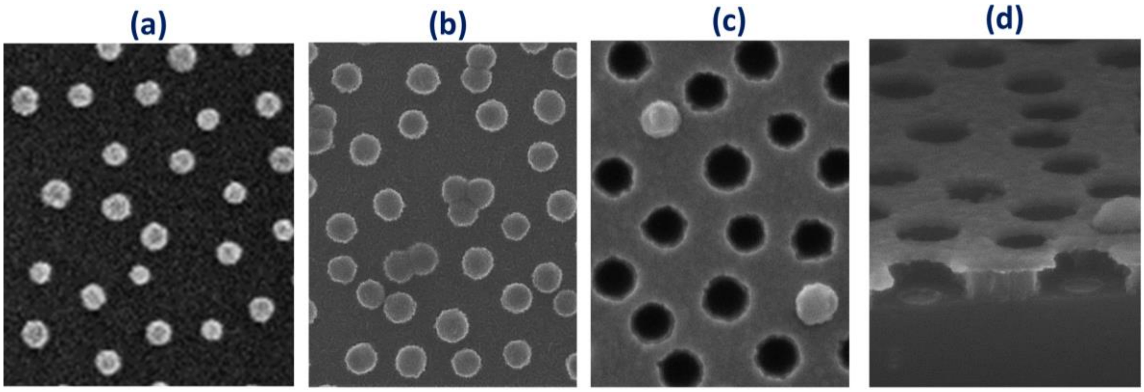

Figure 13 SEM images of several fabrication steps presented in Figure 12 (a) PS nanobeads, corresponds to step (i); (b) The PS nanobeads buried with Cr and Au, corresponds to step (iii); (c) Tape stripping left the Au as the hole mask. Some of the smaller PS retained. This image corresponds to step (iv); (d) The 70^o *view of the undercut, corresponds to step (v).*

The second method employed Cr as the sacrificial layer instead of PMMA used in the first method. The substrate was cleaned with standard cleaning procedure, as explained in the method I. The fabrication steps are described as follows (Figure 12). (i) The PDDA and the PS was deposited within the same procedure as in the previous method. (ii-iii) Afterwards, the chromium thin film of 30 nm thickness, followed by a gold thin film of 15 nm, was deposited by e-beam PVD in sequence. (iv) The PS was removed by tape stripping, leaving the holes in the Au mask. (v) The structure was dipped in water-diluted nickel chromate wet-etch to make the desired undercut. (vi) Afterwards, the Ag of 20 nm thick was deposited by the e-beam PVD to form nanodisk particles. (vii) The Al_2O_3 layer was deposited by ALD to encapsulate the Ag nanodisk. (viii) The final deposition was Pt of 5 Å thickness by e-beam PVD. (ix) Finally, the sacrificial layer and the mask were lifted off by undiluted nickel chromate solution, leaving the final structure printed on the surface.

4.3 Method III: Carbon Sacrificial Layer

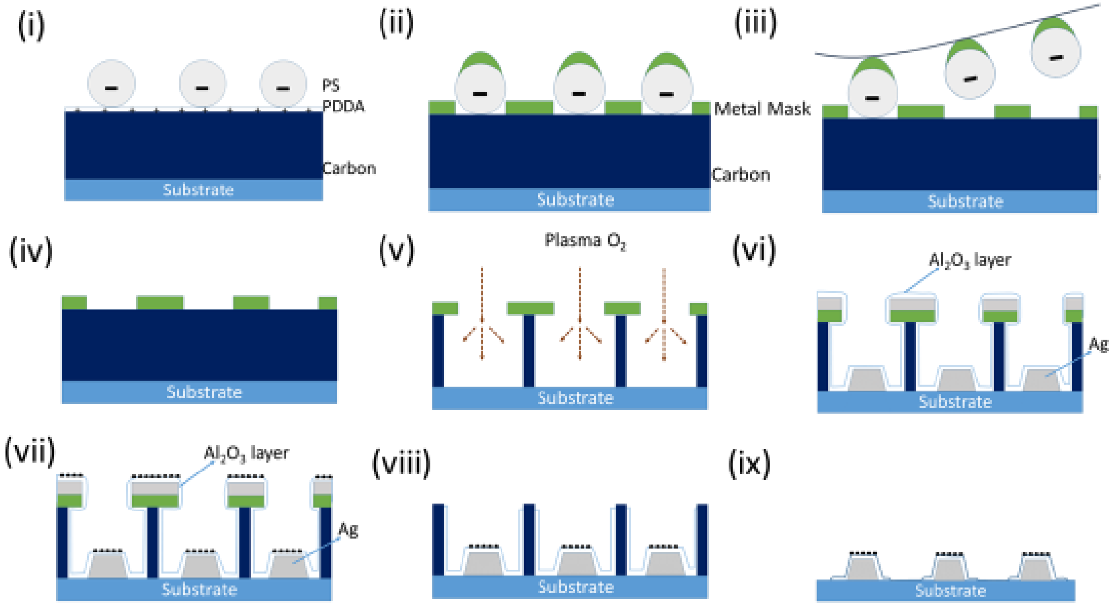

Figure 14 Method III: Fabrication based on carbon as the sacrificial layer.

The third method employed carbon as the sacrificial layer (Figure 14). The same cleaning procedure as for the previous methods was performed before the deposition process. The nanofabrication began with deposition of 30 nm carbon thin film with e-beam PVD (AVAC HVC600), followed by deposition of PDDA and PS solution (i). In this method, we used a metallic thin film i.e. chromium to form the hole-mask, it was deposited by e-beam PVD (ii). Later, the PS was removed by tape stripping, leaving the holes in the Cr mask (iii-iv). The undercut was made by O_2 plasma dry etching (v). Silver of 20 nm thickness was deposited by e-beam PVD followed by 2.5 nm Al_2O_3 ALD deposition (vi). Platinum of 5 Å thickness was deposited by the e-beam PVD afterwards (vii). The lift off process consisted of two steps. Firstly, the mask was removed by undiluted nickel chromate. Secondly, the exposed carbon layer was removed by O_2 plasma.

CHAPTER 5: RESULTS AND DISCUSSION

5.1 Method I (PMMA Sacrificial Layer)

(i) The Structure

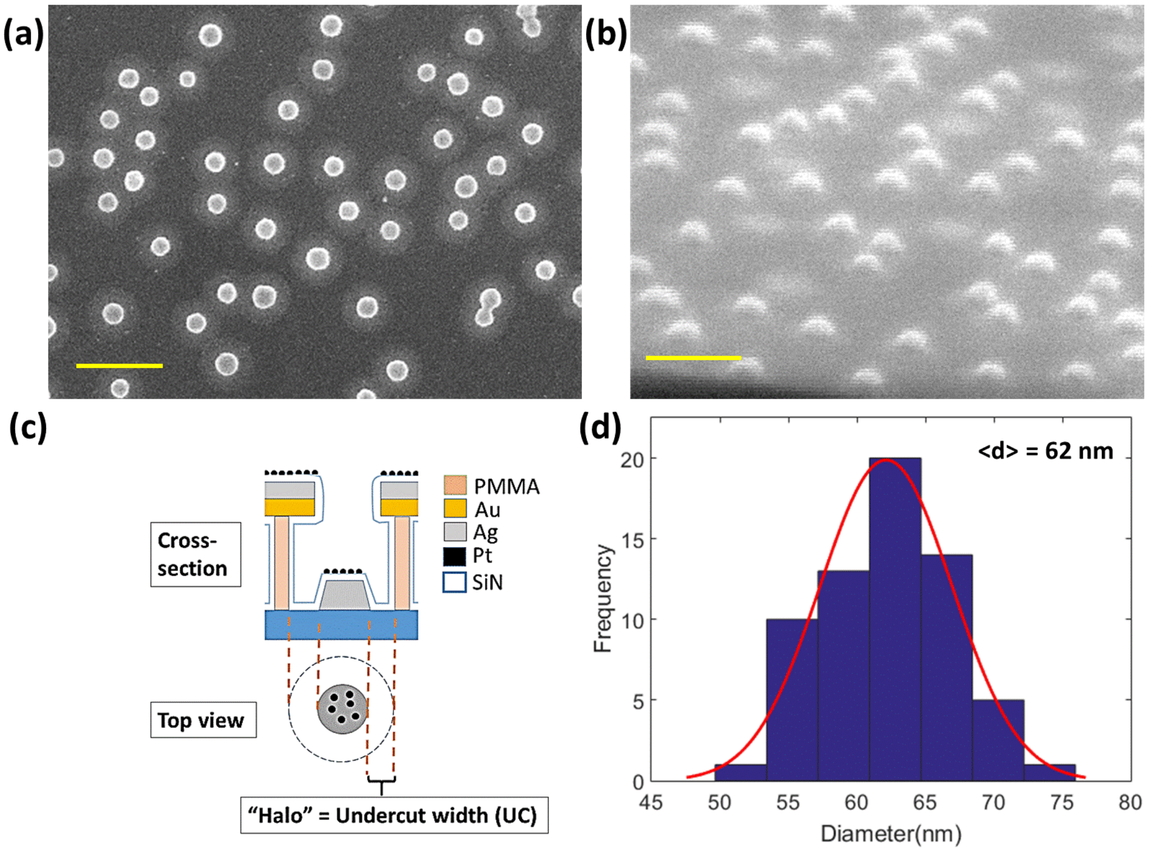

Figure 15 SEM images of the Ag nanodisks covered with 5 nm SiN_x layer: top view (a) and 70^o tilt view (b) (scale bar 200 nm). Pt of 5 Å was deposited on top of the SiN_x-encapsulated nanodisks. The bright circles are the Ag nanodisks while the surrounding halos are the SiN_x layer. The Pt is not visible with the limited resolution of the SEM. The

halo and undercut are illustrated in (c). The Ag nanodisk diameter distribution of the fabricated sample is presented in (d).

SEM images of the fabricated structures are presented in Figure 15(a)-(b). The sample was fabricated with PS of 58 nm and SiN$_x$ deposition for 20 seconds yielding 5 nm thickness. The size distribution of the nanodisks on the substrate was calculated with ImageJ software [33] and is presented in Figure 15(d), which shows that most of the nanodisks are of diameter between $60 - 65$ nm. By Gaussian fit, the average diameter is calculated to be 62 nm. It is 4 nm off from the polystyrene average size of 58 nm. It is also calculated that the nanodisks occupies ca. 10% area of the substrate and the distance between nanodisks is 100 to 200 nm. The coverage was obtained with PS of 0.025 %v of concentration.

The undercut is a crucial part in this fabrication due to several reasons. Firstly, the undercut determines how good the spacer i.e. nitride or oxide covers the easily-oxidized silver. If the undercut width is too narrow, the spacer will not cover the side of the nanodisks. Secondly, a very wide undercut means that plenty of PMMA sacrificial layer beneath the Au mask is etched, which means that there is an increased chance of mask collapse.

The undercut width is assumed to be equal to the width of the SiN$_x$ halo (illustrated in Figure 15(c)). Thus, by measuring halo width, the undercut width can be estimated. With this method, the undercut width of different O_2 plasma dry etching times can documented (Figure 16). The undercut as narrow as 30 nm was achieved by 1 minute and 15 seconds O_2 plasma exposure. The undercut rate seems to be constant until two minutes of etching and become slower afterwards. The reason of the slower rate is because the plasma is driven by a vertical RF field. At a moment when the undercut is wide enough, the plasma need longer time to laterally reach the PMMA wall.

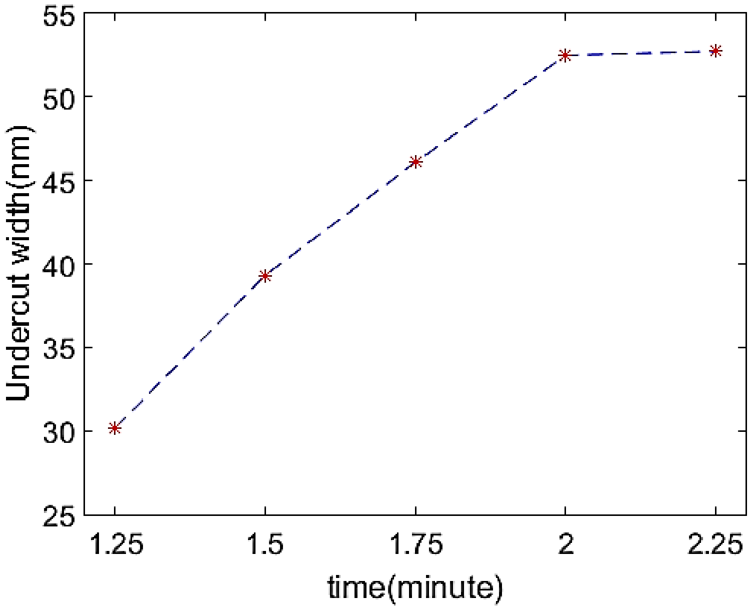

Figure 16 The undercut width versus the plasma etching time.

(ii) The Absorption Enhancement

Sample 1

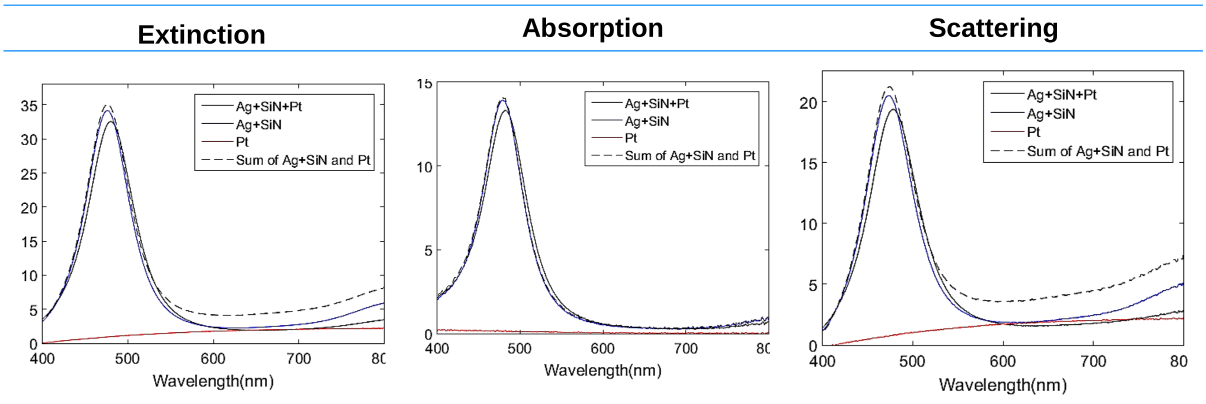
Extinction

Absorption

Scattering

Sample 2

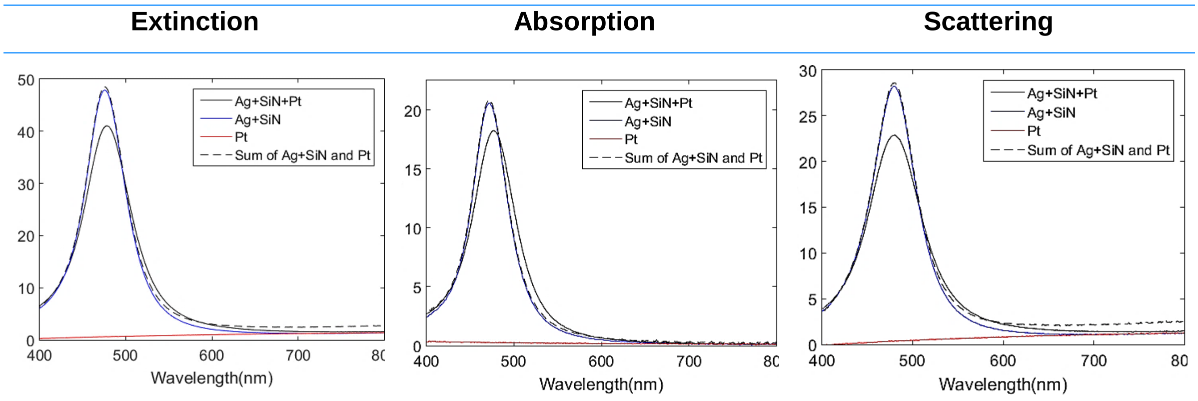
Extinction

Absorption

Scattering

Sample 3

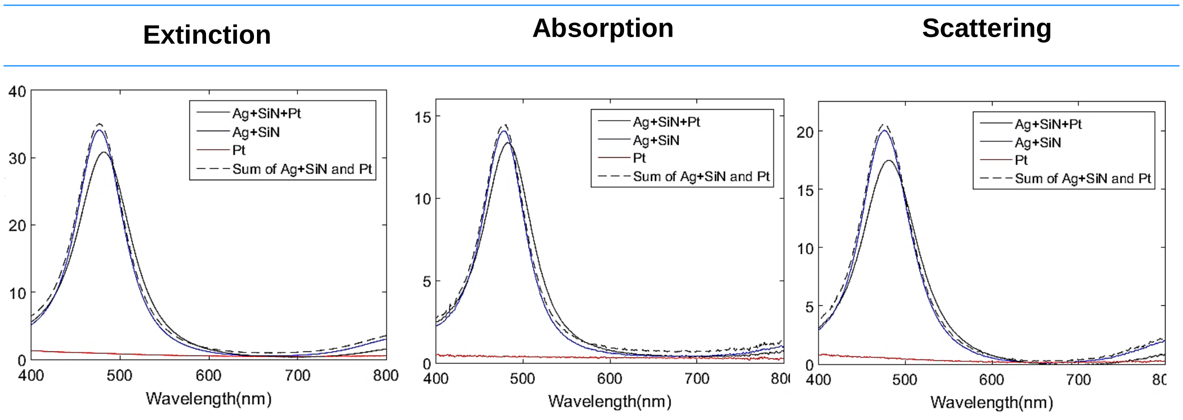
Extinction

Absorption

Scattering

Figure 17 The extinction, scattering, and absorption spectra of the Ag nanodisks of height 20 nm and average diameter ~62nm. The spectra of three samples (fabricated in different batches) are presented. The dielectric spacer is SiN$_x$ of 5nm thickness. The Pt was as a

5 Å thin granular film, which forms small particles due to substrate dewetting. The red line represents the spectra of Pt nanoparticles alone, the blue line represents the spectra of Ag nanodisks covered by SiN_x, the black line represents the spectra of the complete structure (Ag covered with SiN_x and Pt). The dashed-line is the sum of the individual constituents of the structure, i.e. the Pt spectra (red) and the Ag covered SiN_x spectra (blue).

To evaluate the effect of the Ag plasmonic resonance on the absorption of light in the adjacent small Pt nanoparticles, three kinds of samples were fabricated, namely, Pt on SiN_x, SiN_x-covered Ag, and the complete structure of Ag/SiN_x/Pt. The absorption spectra of the different structures are shown in Figure 17. One can observe that the absorption of the complete structure is not the same as the sum of the constituents, i.e. of the Pt nanoparticles alone and of the Ag nanodisks alone. Thus, the absorption of the Ag/SiN_x/Pt coupled structure is not a linear superposition of the constituents' absorption.

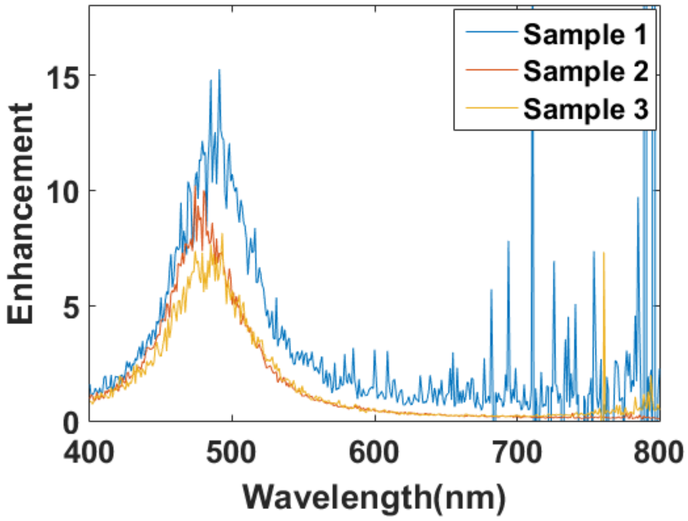

Figure 18 Absorption enhancement in the Pt nanoparticles calculated for the three different samples using a theoretically derived splitting factor for absorption in the Pt and in the Ag[13].

As the Pt is placed in the Ag’s LSPR influence zone, the absorption enhancement can be defined as:

$$E = S\ x\ \frac{Absorption\ of\ Ag + SiN + Pt}{Absorption\ of\ Pt}$$

Where S is the so-called splitting factor, which is a fraction of the field absorbed by the catalyst in the coupled structure. The other fraction of the field ($100\% - S$) is absorbed by the plasmonic nanoparticle. By assuming the splitting factor is 12%, the absorption enhancements of the three samples are calculated and are presented in Figure 18. The splitting factor was taken from FDTD simulations by Antosiewicz et al [13]. However, it should be noted that the splitting factor of our nanostructure might be slightly different, since Antosiewicz et al. calculated the splitting factor for Pd instead of Pt. With this slight reservation, we find that absorption in the Pt nanoparticles is enhanced at least by factor of 8 at wavelength ca. 490 nm, which coincides with the LSPR in the silver nanodisk. Another sample showed enhancement as high as 15 times. This enhancement is lower than the enhancement obtained by Antosiewicz et al. [13]. Apart from the different employed catalyst material, the enhancement difference is likely to come from the fact that our catalyst only decorates the top surface of the nanodisks whereas their catalyst decorated the top and the side (where field enhancement is largest) of the nanodisk, thus exhibiting larger enhancement.

(iii) Oxidation Test

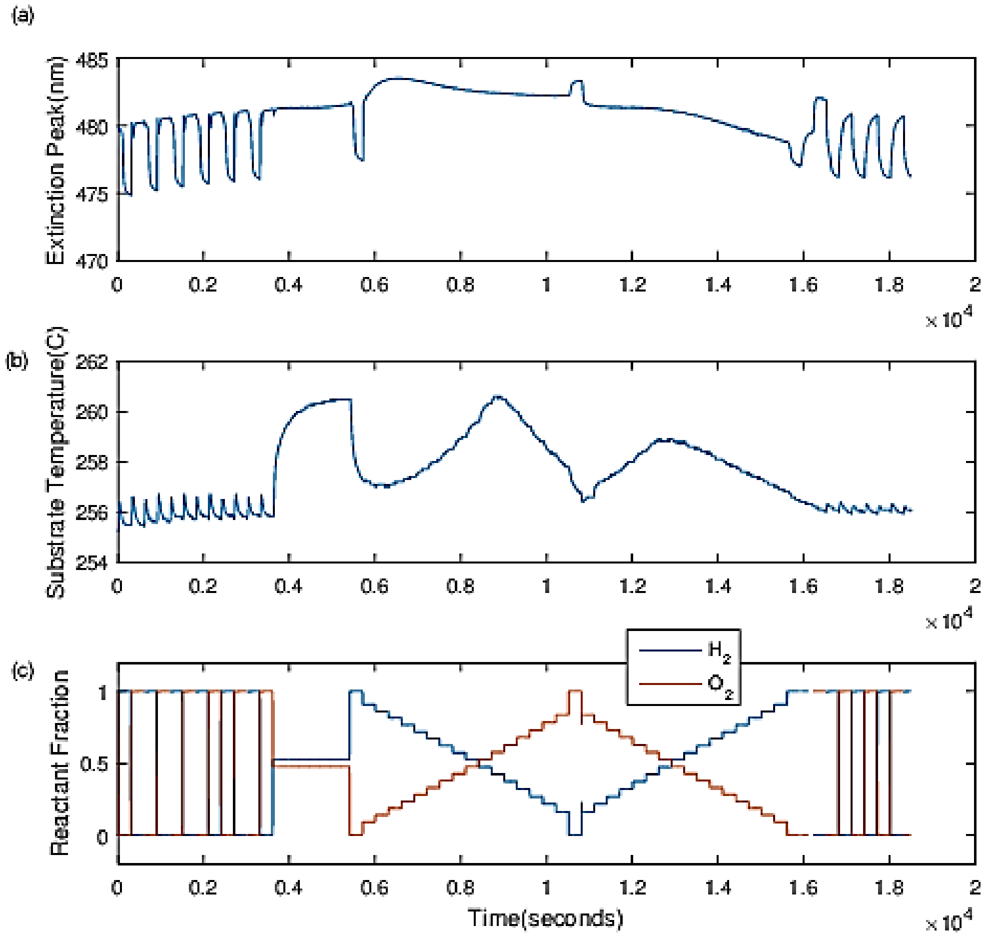

Figure 19 The extinction peak, substrate temperature and gas composition during 5.5 hours of oxidation test. The reactor temperature was set to 320℃.

The oxidation tests were performed on both Ag/SiN$_x$/Pt and Ag/Pt samples to evaluate how good the SiN$_x$ layer protects the Ag nanodisk from oxidation (deterioration) in severely oxidizing (and reducing) conditions. The test was run at five different temperatures: 320 ℃, 400 ℃, 500 ℃ and 600 ℃. The sample was tested within 320 ℃ condition first. If it was not oxidized (indicated by the presence of the LSPR peak at 480 nm after the experiment) at the lower temperature, it would undergo the next higher temperature test condition. For each temperature conditioning, the test was run for 5.5 hours using a 2% mixture of O_2 and H_2 as the reactants diluted in Ar carrier gas.

The total flow of the gases was 190 mL/min. The relative concentrations of the H_2, defined as

$$\alpha_{H_2} = \frac{concentration\ of\ \ H_2}{concentration\ of\ [H_2 + O_2]}$$

, were varied over time (Figure 19(c)). At the relative concentration ($\alpha_{H_2,cr}$) ca. 0.5, the substrate temperature reached a maximum point (Figure 19), an indication of maximum exothermic reaction rate of the hydrogen oxidation reaction promoted by the Pt catalyst. This is thus also an indication that the Pt functions as catalyst, as anticipated [34].

In the end of this test, we found that the Ag that was protected with 5 nm SiN_x was not even completely oxidized after the $600\ ℃$ test. The extinction intensity after the $600℃$ test is approximately a half of the intensity after the $320℃$ test (Figure 20 (left)). The peak position shift is an indication of the refractive index change on the surface of silver nanodisk, which might come from the diffusion of oxygen in to the SiN_x spacer or in to the interface of the SiN_x-Ag to form a new compound. On the other hand, the sample without SiN_x cover is more vulnerable to oxidation. The extinction peak is only 20% i.e a half of the intensity of the sample with SiN_x, in the beginning of the test. The Ag was almost perfectly oxidized after the $600℃$ reactor test (Figure 20 (right)). Hence, the SiN_x spacer increased the oxidation resistance of the silver by approximately factor of two.

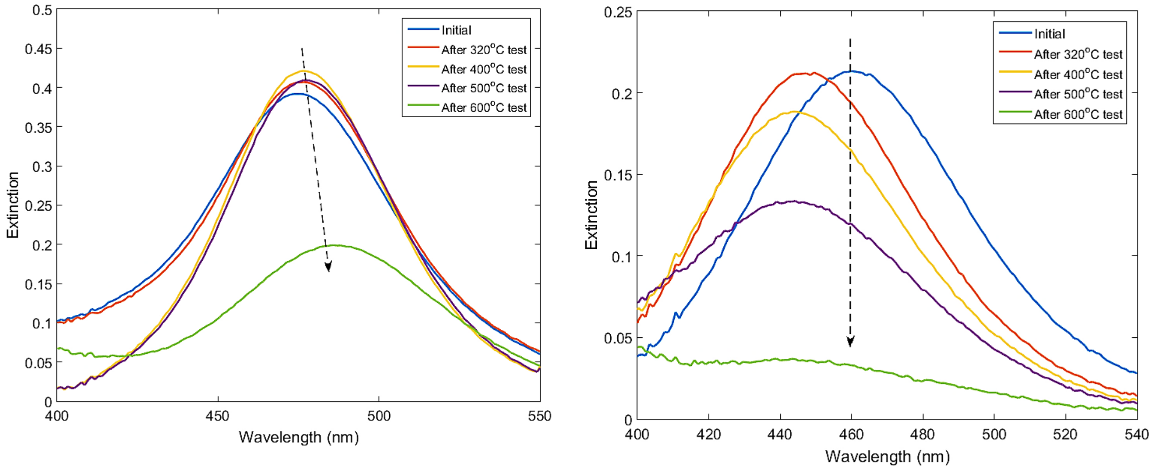

Figure 20 The extinction spectrum after different temperature condition tests of the sample with 5 nm SiN$_x$ spacer (left) and without SiN$_x$.

(iv) Improvement of Method I

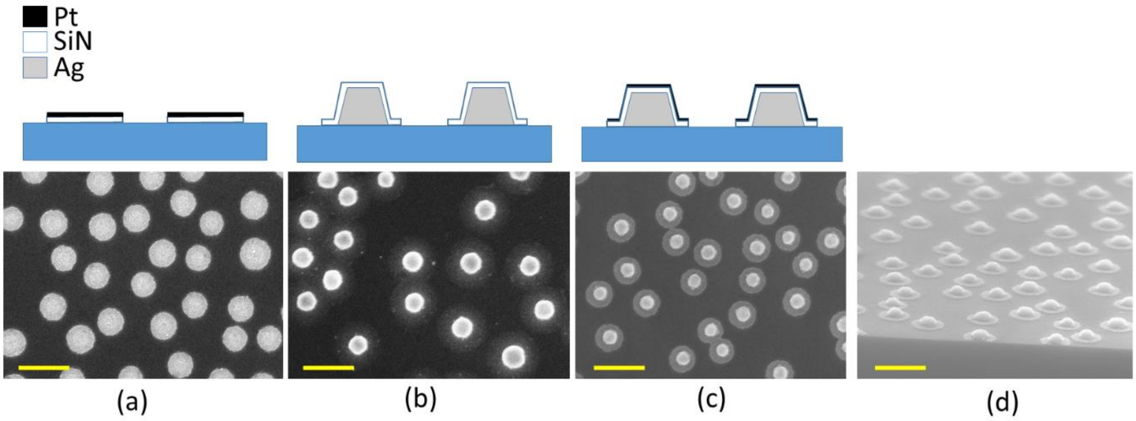

Figure 21 SEM images of the Ag nanodisks (h =20nm, <d>=62nm) encapsulated by a 5 nm SiNx layer and decorated by a 2 nm platinum thin film, as fabricated with the improved method I (scale bar 200 nm). For absorption measurement purpoe, three kinds of structures were fabricated: (a) Pt on SiNx, (b) Ag nanodisks covered by SiNx and (c) the complete structure of Ag, SiNx and Pt. The 70^o tilt image of the complete structure (c) is shown in (d). Each structure is represented by a cartoon above the respective SEM image.

With the method I, the Pt nanoparticles are deposited on the top surface of the Ag nanodiscs only. However, for the absorption enhancement measurement purpose, it is also desirable that the Pt is deposited on the side of the Ag nanodiscs as well, where the enhanced field is maximal. This structure can be attained by removing the Au mask by tape stripping after the PECVD process (see step (vii) in Figure 11) which consequently expose the undercut. Therefore, the subsequent Pt deposition will cover all sides of the nanodiscs with an extra margin surrounding the discs (Figure 21(c)). The Pt margin was recorded to be ca. 25 nm, it was achieved by 75 seconds plasma undercut. Thus, by employing this method, the Pt could be positioned in the enhancement zone of the Ag LSPR, which is ca. 20 nm.

The fabrication steps of Pt on SiN_x patches (the structure presented in Figure 21(a)) was rather different from the fabrication steps of Pt on Ag (the structure presented in Figure 21(c)). We found that the tape stripping after the PECVD did not successfully lift the Au mask. We believed that the PEVCD passivate the wall of the PMMA well as the PECVD precursors penetrate the well with less challenge when the Ag nanodisc was not present. Thus, this passivation might increase the adhesion of the mask to the PMMA. To overcome this, the Au mask was lifted with Au etchant (mixture of KI/I_2 provided by Sunchem AB). The wet etch did not erode the PMMA mold nor the SiN_x (confirmed by SEM image in Figure 22).

N.B. the absorption enhancement measurement of the structure fabricated with the improvement of method I (Figure 21) has not been performed yet due to the low yield of the fabrication on glass substrate. The main cause of the low yield was the low adhesion of the PMMA to the glass. Thus tape stripping, which is intended to remove the Au mask only, also removed the PMMA sacrificial layer.

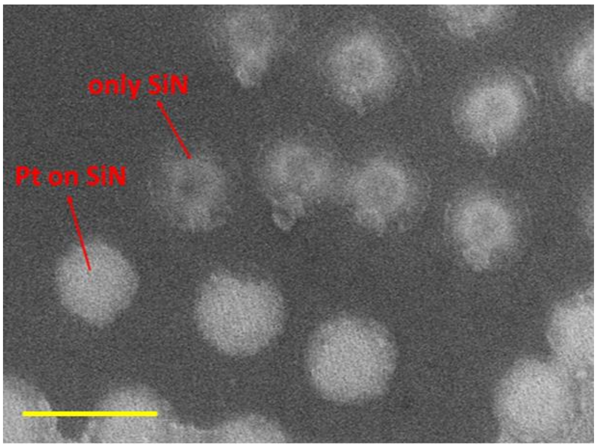

Figure 22 SEM image of Pt on SiN_x patches. In a small area of the sample, some SiN_x circles were not covered by the Pt. The presence of the SiN_x circles indicated that they were not eroded by the Au etchant (scale bar 200 nm).

5.2 Method II (Chromium Sacrificial Layer)

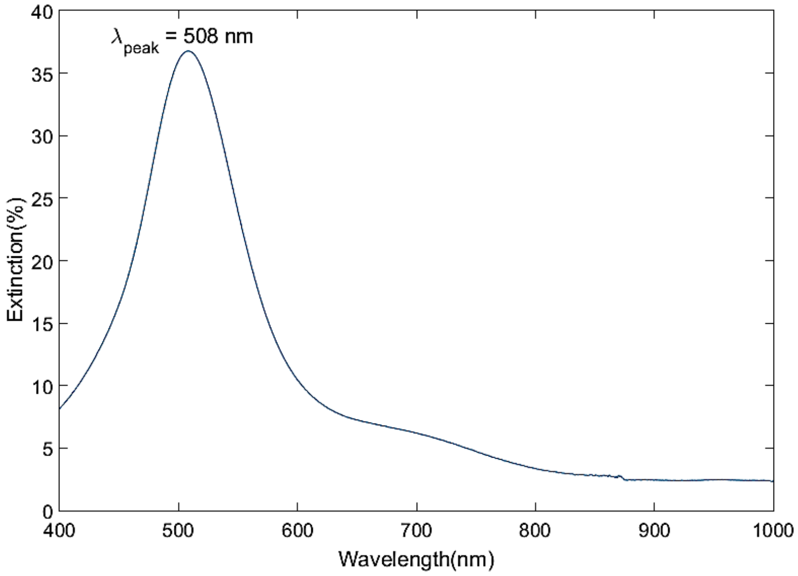

Figure 23 The extinction spectrum of the Ag/Al_2O_3/Pt nanostructures fabricated using chromium as sacrificial layer in HCL. The sample was fabricated using PS nanobeads with 58 *nm diameter. The height of the silver nanodisks is* 20 *nm, the aluminum oxide was deposited with* 21 *ALD cycles (thickness of* 2.5 *nm), and the Pt is of nominally* 5 Å *thickness yielding small nanoparticles due to dewetting. The peak was recorded at* 508 *nm, it is of longer wavelength compared to the sample fabricated with PMMA as sacrificial layer. The reason for this is that the patterned Ag nanodisks by this method turn out to be larger than the diameter of the PS nanobeads defining the mask.*

Reproducible nanofabrication of the complete Ag/Al_2O_3/Pt nanostructures has not been realized in this project. In fact, the complete structure was attained only on one occasion, over a number of trials (the extinction spectra of the only complete sample is presented in Figure 23). The crucial issues that have to be addressed in order to understand the reasons for the regular failure of this method are the undercut and the ALD process since both of them have a crucial impact on the quality of the oxide layer that is to cover the nanodisks. The latter is critical since the lift-off process in this method employs a chromium wet etch which also etches silver, at significant rate. Therefore, the oxide has to completely cover and protect the silver nanodisks from the etchant for the nanofabrication to be successful. Furthermore, the good quality of oxide is also extremely important to protect the silver from oxidation. Here, we discuss some problems that arose from this method.

(i) The Undercut and ALD Problems

In order to achieve a conformal ALD Al_2O_3 layer that encapsulates the Ag nanodisks, the undercut (Figure 12(v)) and the ALD process (Figure 12(vii)) have to be optimized. A large undercut turns out to be very important to make sure that the ALD can cover the side of the nanodisks. Moreover, a certain minimum thickness of oxide has to be deposited by the ALD in order to obtain good protection of the nanodisks from the Cr etchant during the lift off. In principle, the wider the undercut the better the oxide layer encapsulates the nanodisks. However, one should be careful that the undercut is not excessively large because then the Au mask will collapse.

Etchant Concentration and Time

To find the optimized undercut width, the etchant concentration and the etching time were varied. PS nanobeads of 51 nm and 58 nm diameter were deployed in the tests. The rate of the Al_2O_3 300 ℃ plasma ALD deposition is 1.2 Å/cycle, thus we performed deposition of 21 cycles to obtain Al_2O_3 of 2.5 nm thickness. The tested etchant concentration and time variations for the samples fabricated with PS 58 nm are presented in Table 1.

Table 1 Etchant concentration and time variations of the samples fabricated with PS 58 nm nanobeads.

Concentration (Nickel chromate : water)	**Time**
1:6	2 minutes
1:6	2 minutes 30 seconds
1:6	3 minutes
1:3	2 minutes
1:2	1 minutes
1:2	30 seconds

By comparing the number of the “surviving” Ag nanodisks after the lift-off in the Cr wet etchant, we conclude that the best undercut was achieved using 1:3 etchant concentration for two minutes. Note, however, that also in this case a significant fraction of the Ag nanodisks is etched away, as evident from SEM images presented in Figure 26. By measuring the width of the Al_2O_3 halo, it was concluded that the etching leads to an undercut of approximately 25 nm. The size distribution of the nanodisks was quantified with ImageJ [33] and then fitted with Gaussian distribution formula. The average diameter of the nanodisks is 87 nm, which means it is 29 nm larger than the average diameter of the PS nanobeads that are used to define the mask.

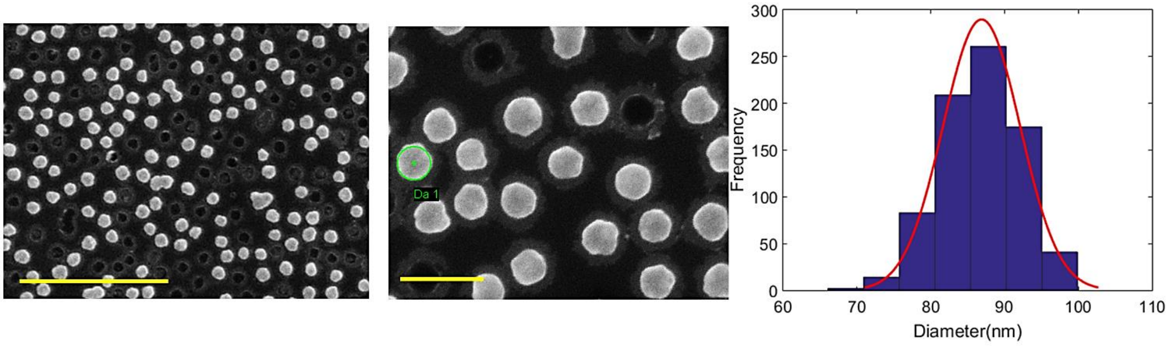

Figure 24 SEM images of a sample fabricated with PS 58 nm: 50k magnification (left, scale bar $1\ \mu m$) and 365k magnification (center, scale bar $200\ nm$). The bright circles are the Ag nanodics whereas the surrounding halo is the Al_2O_3 spacer. The expected oxide thickness was 2.5 nm. The halos without the bright particles indicate the Ag nanodisks were etched away during the lift-off. The nanodisks distribution is presented on the right side. The red curve is a Gaussian fit to the histogram. The average diameter of the nanodisks is 87 nm.

On the other hand, other etching recipes presented in Table 1 resulted in an even lower yield of intact and encapsulated Ag nanodisks. With a more diluted concentration, $1{:}6$ for 3 minutes, more than a half of the Ag nanodisks did not survive. The measured undercut width was around 15 nm. With the same concentration but shorter time, 2 minutes 30 seconds, the measured undercut width was ca. 7.5 nm and the yield of Ag nanodisks was essentially zero (Figure 25). Thus, we can conclude that to have good ALD-deposited oxide, an undercut of at least 15 nm is required.

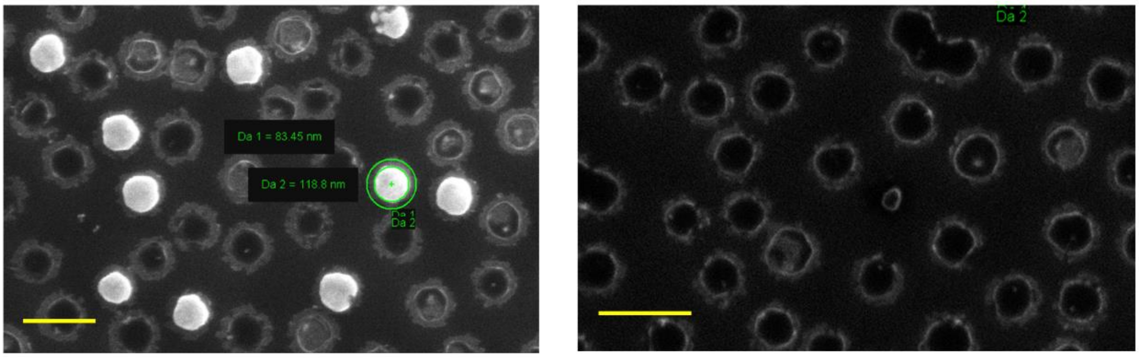

Figure 25 200k-magnification SEM images of the samples fabricated with PS 58 and 1:6 etchant concentration (scale bar 200 nm). The sample etched with etching time of 3 minutes is shown on the left and of 2.5 minutes on the right. The expected oxide thickness is 2.5 nm.

With the similar test, for the samples fabricated with PS 51, we found that the optimized etchant concentration and time was $1{:}6$ for 2 minutes. The obtained undercut width by this recipe was approximately 30 nm. The SEM images of the obtained structures are shown in Figure 26, where one can see that almost all Ag nanodisks survived and that they had an average diameter of 82 nm average diameter, i.e. 31nm larger than the average diameter of the PS nanobeads used to define the mask.

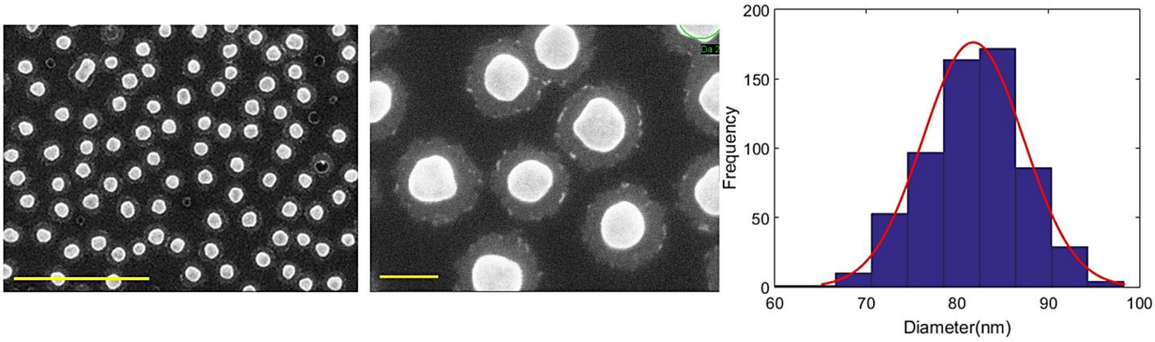

Figure 26 SEM images of the sample fabricated with PS 51 nm: 50k magnification (left, scale bar $1\ \mu m$) and 365k magnification (center, scale bar $200\ nm$). The bright circles are the Ag nanodics whereas the surrounding halo is the Al_2O_3 spacer. The expected oxide thickness was 2.5 nm. The nanodisk size distribution is presented on the right side. The red curve is a Gaussian fit to the distribution. The average diameter of the nanodisks is 82 nm.

The reproducibility rate of samples made with this method was very low. The close-to-ideal structures as presented in Figure 24 and Figure 26 were successfully fabricated at only a small number of occasions among a number of trials using exactly the same recipes.

ALD Process Problem

The wide undercut is not the only issue to overcome in order to obtain good coverage of the oxide on the Ag nanodisks. There were some cases where the Ag did not survive the liftoff although the undercut was large enough. One example of such a situation is presented in Figure 27. The undercut of the sample is ca. 25 nm and the oxide was deposited by 42 cycles to obtain 5 nm of thickness. However, most of the Ag nanodisks did not survive after the lift-off. Hence, we speculated that the imperfect ALD process might contribute to the failure.

As the increase of the ALD cycle number did not affect the number of the surviving Ag nanodisk, we believed that the exposure time of the ALD precursors was too short, provided that the precursors have to access a structure positioned under a hole of ca. 80 nm of diameter. The failure of the plasma ALD to coat high aspect-ratio nanostructures is quite well known. One of the reasons of the poor conformality might be caused by the recombination of the generated radicals and ions before they reach the remote sites [35]. The exposure time (T) is crucial as it scales as $T \propto \left(\frac{L}{d}\right)^2$, where the L and d are denoted for the length and the diameter of the nano-well, respectively [25]. Moreover, another way to improve the conformality in high aspect-ratio structures is by increasing the chamber pressure to shorten the mean free path of the radicals or ions, which consequently increases the probability to access remote sites [25].

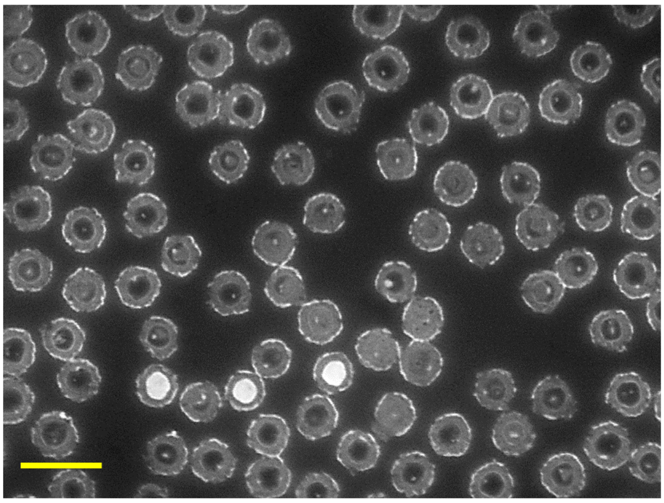

Figure 27 SEM image of a sample fabricated with PS 58. The bright circles are the Ag nanodisks whereas the surrounding halos are the Al_2O_3 film (scale bar 200 nm). The oxide was deposited with 42 cycles to yield 5 nm thickness.

In general, the lift-off process took $15-30$ minutes. In a different test, we deposited Al_2O_3 on a silicon substrate and exposed it to undiluted chromium etchant for 30 mins. By using ellipsometry, we found that there was barely any reduction of the thickness before and after the etchant exposure. Therefore, it is unlikely that the low survival rate of the Ag nanodisks was due to the erosion of the Al_2O_3 by the nickel chromate.

The Thickness of the Cr Sacrificial Layer

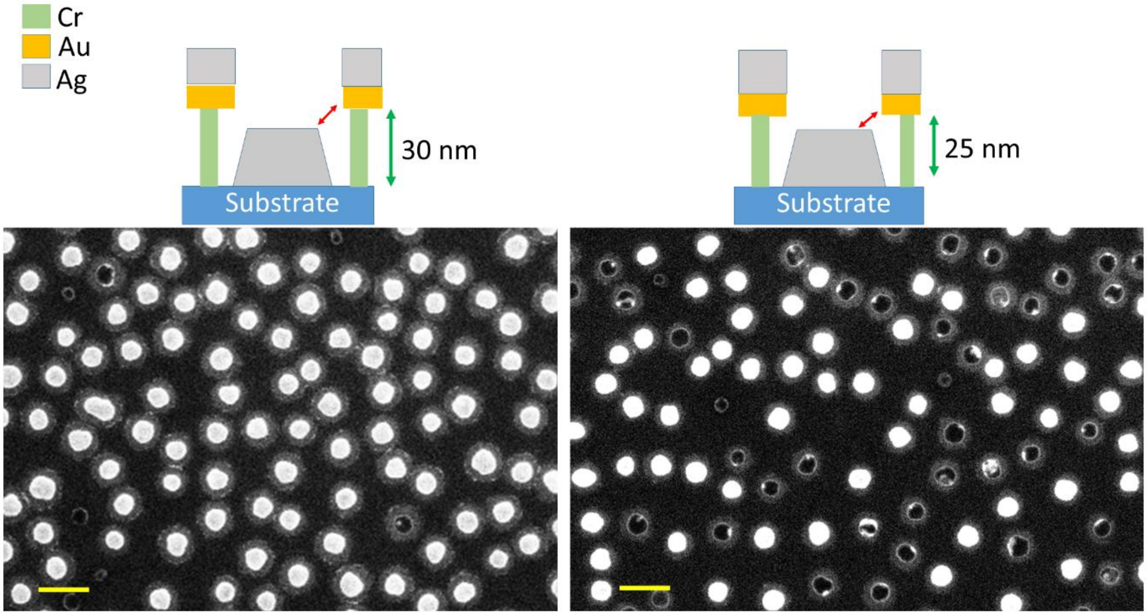

Figure 28 SEM images of oxide-covered Ag nanodisks (scale bar 200 nm). The samples were fabricated using a 30 nm (left) and 25 nm (right) chromium sacrificial layer, respectively. Cartoons of the different thickness of Cr deployed in the fabrication are shown above the SEM images. The red double-headed arrows depict the gap between the top edge of the nanodisk and the edge of the hole mask.

The thickness of the chromium sacrificial layer plays a crucial role for the ALD deposition process. A thick layer will consequently decrease the probability of the ALD precursors to access the base of the nanohole. On the other hand, one has to make sure that the sacrificial layer is not too thin because the top edge of the nanodisks will be too close to the edge of the Au hole mask and thus block precursor penetration into the hole.

I compared the number of the surviving Ag nanodisks fabricated with different thicknesses of the chromium sacrificial layer (Figure 28). They were fabricated with PS of 51 nm diameter and 21 cycles of plasma ALD. The height of the Ag nanodisks was 20 nm. The number of the surviving Ag nanodisks was significantly lower in the sample fabricated with the 25 nm chromium sacrificial layer compared to the 30 nm one. This indicates that a smaller gap between the edge of the nanodisk and the edge of the Au hole blocks the flow of the ALD precursors towards the remote side of the nanodisk. We therefore conclude that 30 nm was a better thickness to compromise the aforementioned restrictions.

(ii) Limit of The Ag Diameter

Larger Hole

We investigated the nanohole size in the mask layer after tape stripping to understand the reason of larger margin between the diameter of the patterned Ag nanodisks and the diameter of PS nanobeads used to define the mask. Using PS 51nm nanobeads, the mask’s hole diameter was measured after tape stripping. Both Au and SiN_x thin films were deployed as masks in this test. With the Au mask, the hole diameter was measured to be ca. 80-100 nm which is larger than PS diameter of 51 nm (Figure 29(left)). This happened due to the periphery of the PS beads pulling of some Cr sacrificial layer and Au mask during the tape stripping. Later, SiN_x - a harder material than Au - was used as mask to observe if the hole diameter could be smaller (Figure 29(right)). However, we found that the hole diameter was very similar to the one obtained when using the Au mask.

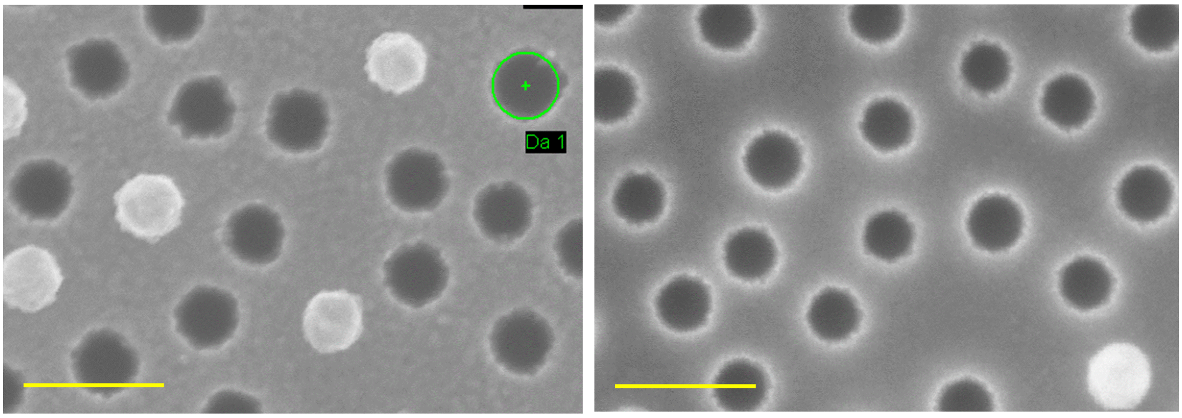

Figure 29 SEM image of the Au mask (left) and the SiN$_x$ mask (right) after tape stripping. The samples were fabricated with PS 51 nm, 30 nm Cr sacrificial layer 30 nm and 15 nm Au or SiNx mask (scale bar 200 nm). Note the basically identical hole size in the mask after tape stripping for the two materials.

In the beginning, the breaking or bending of the hole's periphery after undercut was hypothesized as the contributor to the large difference between PS diameter and the patterned Ag nanodisk. However, by 70° SEM imaging, the alleged bending or the breaking of this periphery can be concluded as non-existing (Figure 30). The diameter of the hole was found to be approximately the same before and after the undercut process. Thus, the larger diameter of the Ag nanodisks is a consequence of the fact that the hole mask is enlarged during the tape stripping step due to the PS nanobead pulling off some of the mask layer.

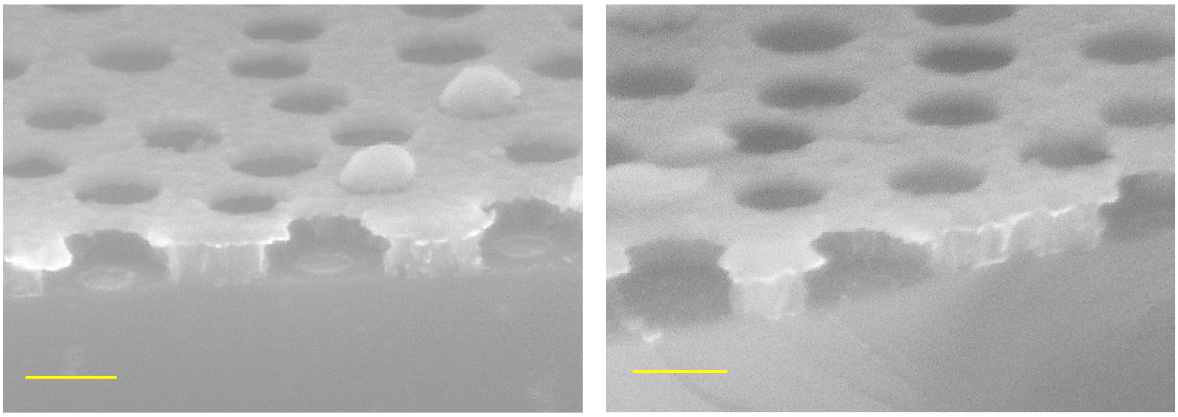

Figure 30 70^o tilt SEM image of the nanohole cross section. The samples were fabricated with PS 51 nm, 30 nm Cr sacrificial layer and 15 nm Au mask. The undercut was made with 1:6 diluted etchant for 2 min (scale bar 100 nm).

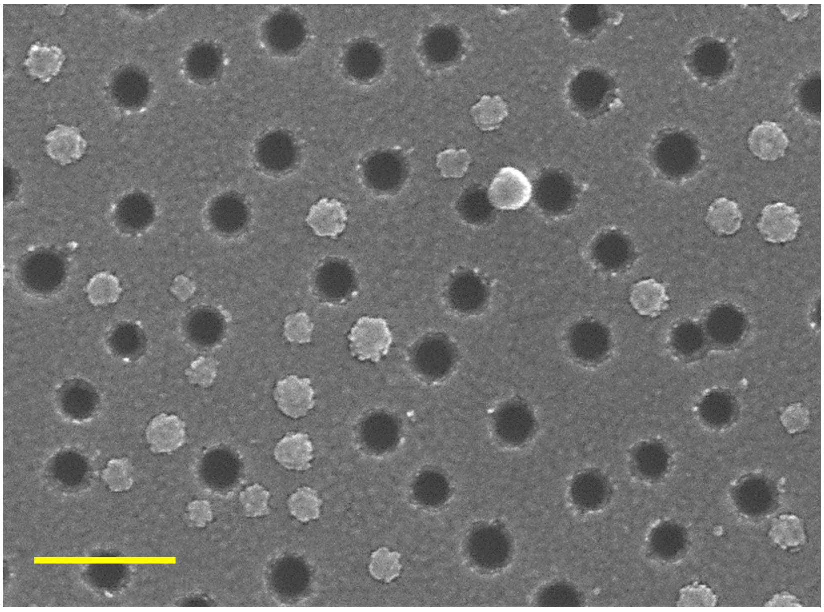

Figure 31 SEM image of sample fabricated using 41 nm sized PS nanobeads. The sacrificial layer was 25 nm Cr and the mask was 10 nm. The black circles correspond to holes that were successfully tape stripped whereas the brighter circles are the Au-covered PS nanobeads that cannot be stripped off. (scale bar 200 nm).

Another problem with this method is that there is a limitation for the use of smaller PS nanobeads in the fabrication, to obtain smaller Ag nanodics. Since the Cr sacrificial layer has to be kept at least at 25 nm thickness (thinner sacrificial layer will results in narrower gap between the nanodisk's and hole's edge, see the discussion in page 52), smaller PS nanobeads (present because of the inherently broad size distribution of the used beads) will be buried too deeply in the Cr sacrificial layer ($25 - 30$ nm) and the Au mask ($10 - 15$ nm) to be removed by the tape stripping. Consequently, there is a significant number of nanobeads, which remains stuck after the tape stripping (Figure 31).

For the same sample, we subsequently performed a second tape strip, as well as sonication in IPA for 20 minutes (10 minutes of gentle power (40W) followed by 10 minutes of harsh power (120W)) and O_2 plasma exposure for 10 minutes in an attempt to remove the remaining PS nanobeads. However, neither the PS nor the Au cap were successfully removed.

5.3 Method III (Carbon Sacrificial Layer)

The use of carbon to fabricate the Ag/spacer/Pt nanostructures is motivated by the shortcomings of PMMA and Chromium as the sacrificial layers. As discussed earlier, PMMA is not a stable material in high temperature, thus a high quality ALD - which is usually attained by heating the support to $300\ ℃$ - is not possible. It is also worth noting that the ALD is preferred over PECVD in the envisioned application for the spacer layer deposition because, theoretically, it provides better material conformity (step coverage) and more accurate thickness control down to the nm level. On the other hand, the chromium sacrificial layer has a disadvantage as the size of the patterned Ag nanodisks is always significantly larger than the size of the PS nanobeads used, limiting the nanostructure size to ca. 80 nm and above.

Since carbon is thermally stable at $300\ ℃$, it is compatible with the ALD process. Furthermore, carbon has a desired similarity with PMMA since it can be dry-etched with oxygen plasma, thus the undercut process similar to the method with PMMA can be adopted. With these advantages, in principle, it should be possible to nanofabricate Ag nanostructures with the targeted size and with a thin conformal oxide encapsulation grown by ALD. However, unlike for PMMA, carbon lift-off is not well documented. Strong acids or bases have been reported to wet-etch carbon, but only at the boiling temperature [36].

To avoid those wet etchants, I tested two alternative strategies to first remove the metal mask from the carbon sacrificial layer (prior to dry etching the carbon by oxygen plasma): (i) tape stripping; (ii) wet etching. To facilitate the former strategy, a metal with low adhesion to carbon should be chosen. To test which metal(s) that would exhibit low adhesion to an evaporated carbon layer, bilayer samples of carbon (30 nm) and metal (15 nm) were prepared. Afterwards, tape stripping and ten minutes ultrasonication (5 minutes of gentle and 5 minutes of harsh power) were performed to see the possibility to remove the metal from the carbon film. The used metals were Ti, Cr, Al, Au, Ge, Pd, Ni, Pt, Ag and Cu. However, none of those metals showed low enough adhesion to carbon. The tape stripping and the ultrasonication did not remove the carbon layer from the substrate either. Therefore, a wet-etching step to remove the metal mask is unavoidable.

The first trial was to use chromium as the mask because the etching is similar to the method with chromium sacrificial layer described above. Samples with different undercut were made with oxygen plasma of 50 W power, 250 mTorr pressure, and 10 sccm oxygen flow. I previously had measured the etch rate of carbon thin films by the generated oxygen plasma and concluded that it removed carbon thin film with the rate of ca. $10\,nm/min$. I thus tried etching times varying from $4 - 8$ minutes. However, none of the samples had a wide enough undercut. For instance for the sample with 6 minutes of plasma etching shown in Figure 32, the average undercut diameter was recorded as 70 nm. Thus by assuming that the hole-mask diameter is the same as the average diameter of the used PS nanobeads of 58 nm, we conclude that the undercut margin is 12 nm. In other samples with longer etching time i.e. 8 minutes, the undercut margin is approximately the same as found for the undercut of 6 minutes etching. N.B. longer time etching times up to 14 minutes have also been tried but in the end the expected oxide-encased Ag structures were not successfully formed. There were two possible causes: the undercut margin was not increased or the mask collapsed.

The latter scenario is unlikely because had the mask collapsed, the Cr mask lift-off would not have been successful either. If the former was the cause, in the future I suggest that the oxygen plasma of low RF power, higher pressure and higher flow is utilized to make the undercut. This will generate plasma of shorter mean free path and thus increase the lateral carbon etch rate.

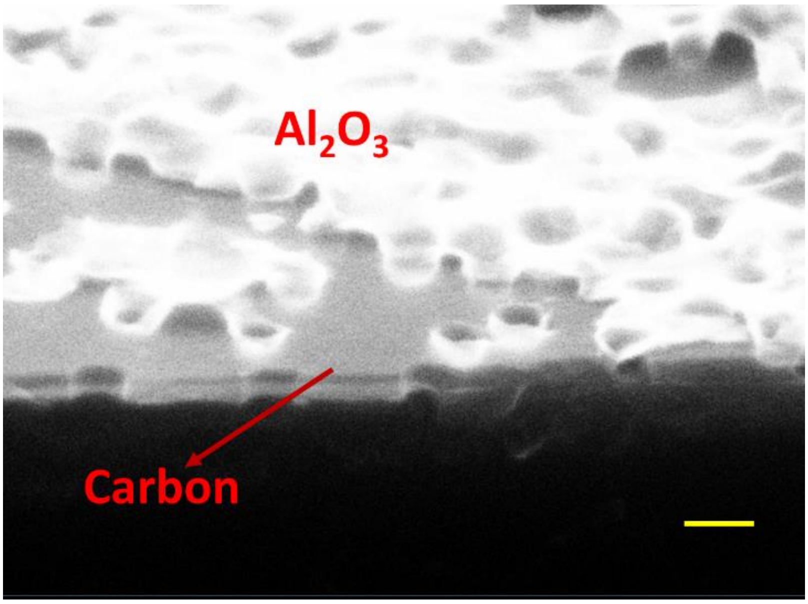

Figure 32 The nanoholes after the wet-etching of the Cr mask. In certain areas, carbon was exposed but on the other areas the Al_2O_3 *was still in place (scale bar 200 nm).*

Since the undercut was too small, Al_2O_3 was also deposited on the wall of the carbon hole during ALD. Consequently, the oxide stayed in place after the Cr mask lift-off (Figure 32). The sample in Figure 32 was later underwent the second step of lift-off: carbon removal by oxygen plasma (Figure 33).

As shown in Figure 33, the carbon remained in place on the areas where it was encapsulated by the oxide. This comes about because in the oxygen plasma etching (10 minutes) only the exposed carbon is removed, leaving vertical Al_2O_3 “flakes” on the surface. One can also notice that the Ag nanodisks did not “survive” since they were etched away by the Cr etchant.

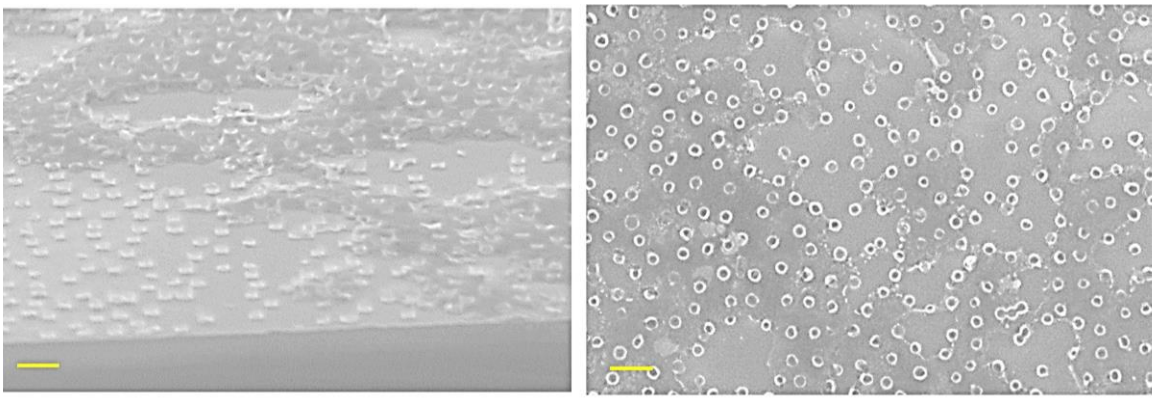

Figure 33 The sample after the exposure to oxygen plasma to remove the carbon sacrificial layer. The darker area indicates that the carbon was still present on the surface due to protection by the unremoved Al_2O_3. In the brighter areas the carbon film has been removed, leaving a ring-like Al_2O_3 structure that previously had coated the nanohole's wall (see Figure 32). The left image is the 70° tilt view whereas the right image is the top view (scale bar 200 nm).

In the last type of samples tried, we tested a Cr-Au bilayer thin film as the hole-mask with the idea that additional strain in the mask, induced by the bilayer architecture, would assists in creating cracks in the oxide layer during the Cr etch, thereby making the mask accessible for the etchant (Figure 34). As seen when analyzing the test sample made, this approach indeed made it possible to completely remove the Al_2O_3 layer and the metal mask from the carbon sacrificial layer, which in turn was totally removed after oxygen plasma exposure.

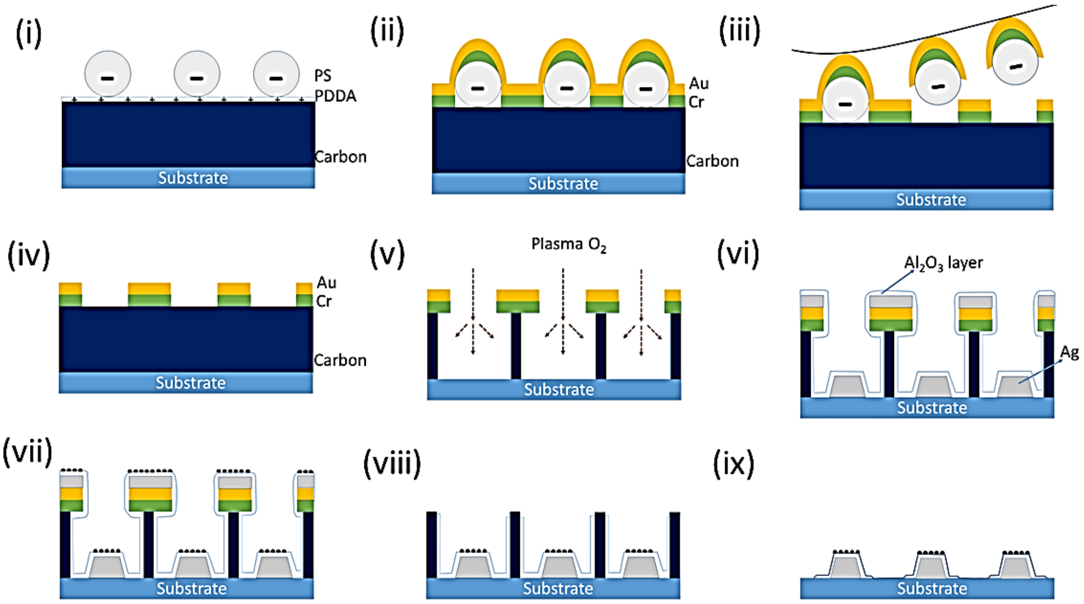

Figure 34 Bilayer metal masks to assist the oxide removal via strain-induced cracks. In this case the bilayer layer was composed of chromium and gold. The gold was deposited after the chromium deposition. The thickness of the metals were 15 *nm each.*

CHAPTER 6: CONCLUSIONS AND OUTLOOK

By modifying the standard hole-mask colloidal lithography nanofabrication method, the targeted nanostructures comprised of an array of sub-100 nm silver nanodisks encapsulated by a few nm thin silicon nitride layer and decorated with small platinum catalyst nanoparticles have been successfully fabricated. Specifically, using *method I* with PMMA as the sacrificial layer and PECVD to deposit the silicon nitride, structures comprised of plasmonic Ag nanodisks with average diameter of nanodisk 62 nm and height of 20 nm, covered by 5 nm silicon nitride, have been made and proven to protect the silver nanodisks from oxidation at temperature as high as 600 ℃.

For these nanostructures the optical absorption enhancement in the platinum nanoparticles due to the LSPR of the silver nanodisk was found to be at least a factor of 8, by assuming the splitting factor of 12% (from [13]). To this end, the spirit of harvesting solar energy mentioned in the beginning of this report is possible to attain, given that the maximal enhancement occurred at wavelength of ca. 490 nm, at which the solar power is the most abundant. The absorption enhancement should have been higher if the platinum nanoparticles had been deposited on all over the surface of the nanodisk. The structure of this type has been demonstrated, by slight modification of the method. The absorption enhancement measurement of such structure would be interesting for the next project.

The other two methods tested, employing a chromium and carbon sacrificial layer, respectively, have not successfully fabricated the desired structure with sufficient yield. The reproducibility of the method II (chromium as sacrificial layer) was very low, as the consequence of the undercut and the ALD process uncertainty. Both of the processes are crucial to obtain perfect coverage of the oxide to the nanodisks. The instability of the undercut process might have come from manual operations e.g. etchant dilution, etching timing, i.e. “the human factor”. This means that further improvements should be possible by further optimizing the whole process. It is also worth noting that dry chromium etching is an alternative way to try, because the etchant mixture and etching timing can be controlled automatically. N.B. the chromium dry etching process is available in the tool#404 (Oxford Plasmalab System 100) in the cleanroom. Furthermore, the ALD process can be improved by prolongation of precursor exposure and products purge time. Another possible way is to raise the process chamber pressure to allow the precursors to reach the most remote areas inside the nanoholes of the mask. It is also important to note that method II has limitation to pattern accurate nanodisk size (compared to the size of PS).

The method III (carbon as sacrificial layer) has a disadvantage as it requires a two-steps lift-off process: (i) removal of the upper metal mask and (ii) removal of the carbon layer. Another issue with this method was the difficulty to make large enough undercut, at least with oxygen plasma of 50 W power, 250 mTorr pressure, and 10 sccm flow. I therefore suggest a low power, higher pressure, and higher flow plasma to increase the lateral etching rate, for future fabrication attempts using this method. It is also worth noting that the carbon method has the potential to circumvent the size accuracy issue of the chromium method and is therefore worth pursuing further.

In summary, despite not fully succeeding within the given time frame of this master thesis, there are chances to obtain the desired structures with both the chromium and the carbon sacrificial layer methods by exploring my suggestions made above. The main motivation for attempting to get at least one of these methods to work is their compatibility with ALD processing of the encapsulating layer. Since very precise deposition of oxide is in principle possible with ALD, one could in the future try to observe how the thickness of the oxide influence the absorption enhancement. Furthermore, ALD supports deposition of high-k oxides such as hafnium oxide. It would be interesting to observe the absorption enhancement of structure with the high refractive index oxide experimentally since theory predicts a direct correlation between spacer layer refractive index and absorption enhancement in the catalyst nanoparticles.

Finally, I would like to note that, in spite of the failure of method II and method III to fabricate the desired structures with sufficient yield, there were a number of interesting fabrication insights that came along the trials. I hope that these findings will be useful for further nanofabrication projects. Speaking about future prospects, the fabricated structure is not only useful for absorption enhancement of catalyst nanoparticles. With the developed methods, it is possible to deposit functional materials *exclusively* in the LSPR field. For example, such a material can be tailored to selectively bind molecules exclusively in the LSPR zone. It is also possible to use the well-protected plasmonic nanoantenna for sintering or catalytic reaction studies on a single particle in harsh environment.

REFERENCES

[1] M. L. Brongersma, N. J. Halas, and P. Nordlander, "Plasmon-induced hot carrier science and technology," *Nat. Nanotechnol.*, vol. 10, no. 1, pp. 25–34, 2015.

[2] K. M. Mayer, J. H. Hafner, and A. À. Antigen, "Localized Surface Plasmon Resonance Sensors," pp. 3828–3857, 2011.

[3] K. A. Willets, R. Van Duyne, and R. P. Van Duyne, "Localized Surface Plasmon Resonance Spectroscopy and Sensing," *Annu. Rev. Phys. Chem.*, vol. 58, no. 1, pp. 267–297, 2007.

[4] L. B. Sagle, L. K. Ruvuna, J. a Ruemmele, and R. P. Van Duyne, "Advances in localized surface plasmon resonance spectroscopy biosensing.," *Nanomedicine (Lond).*, vol. 6, no. 8, pp. 1447–62, 2011.

[5] L. Vinet and A. Zhedanov, *Nanoplasmonic Sensors*, vol. 44, no. 8. New York, NY: Springer New York, 2012.

[6] S. Linic, P. Christopher, and D. B. Ingram, "Plasmonic-metal nanostructures for efficient conversion of solar to chemical energy," *Nat. Mater.*, vol. 10, no. 12, pp. 911–921, 2011.

[7] P. Christopher, H. Xin, and S. Linic, "Visible-light-enhanced catalytic oxidation reactions on plasmonic silver nanostructures," *Nat. Chem.*, vol. 3, no. 6, pp. 467–472, 2011.

[8] S. Mukherjee, F. Libisch, N. Large, O. Neumann, L. V Brown, J. Cheng, J. B. Lassiter, E. a Carter, P. Nordlander, and N. J. Halas, "Hot Electrons Do the Impossible: Plasmon-Induced Dissociation of H2 on Au," 2012.

[9] S. Shen and S. S. Mao, "Nanostructure designs for effective solar-to-

hydrogen conversion,” *Nanophotonics*, vol. 1, no. 1, pp. 31–50, 2012.

[10] Y. Kim, D. Dumett Torres, and P. K. Jain, “Activation Energies of Plasmonic Catalysts,” *Nano Lett.*, vol. 16, no. 5, pp. 3399–3407, May 2016.

[11] T. J. Antosiewicz and S. P. Apell, “Optical enhancement of plasmonic activity of catalytic metal nanoparticles,” *RSC Adv.*, vol. 5, no. 9, pp. 6378–6384, 2015.

[12] T. J. Antosiewicz, S. P. Apell, C. Wadell, and C. Langhammer, “Absorption enhancement in lossy transition metal elements of plasmonic nanosandwiches,” *J. Phys. Chem. C*, vol. 116, no. 38, pp. 20522–20529, 2012.

[13] T. J. Antosiewicz, C. Wadell, C. Langhammer, T. J. Antosiewicz, C. Wadell, and C. Langhammer, “Plasmon-Assisted Indirect Light Absorption Engineering in Small Transition Metal Catalyst Nanoparticles,” pp. 1591–1599, 2015.

[14] T. J. Antosiewicz, S. P. Apell, C. Wadell, and C. Langhammer, “Optical activity of catalytic elements of hetero-metallic nanostructures,” vol. 9502, p. 95020D, 2015.

[15] M. K. Kumar, S. Krishnamoorthy, L. K. Tan, S. Y. Chiam, S. Tripathy, and H. Gao, “Field Effects in Plasmonic Photocatalyst by Precise SiO 2 Thickness Control Using Atomic Layer Deposition,” *ACS Catal.*, vol. 1, no. 4, pp. 300–308, 2011.

[16] X. Zhang, X. Ke, A. Du, and H. Zhu, “Plasmonic nanostructures to enhance catalytic performance of zeolites under visible light.,” *Sci. Rep.*, vol. 4, p. 3805, 2014.

[17] H. Fredriksson, Y. Alaverdyan, A. Dmitriev, C. Langhammer, D. S. Sutherland, M. Zäch, and B. Kasemo, “Hole-mask colloidal lithography,” *Adv. Mater.*, vol. 19, no. 23, pp. 4297–4302, 2007.

[18] G. V. Naik, V. M. Shalaev, and A. Boltasseva, “Alternative plasmonic materials: Beyond gold and silver,” *Adv. Mater.*, vol. 25, no. 24, pp. 3264–3294, 2013.

[19] N. W. Aschcroft and N. D. Mermin, *Solid State Physics*, 1st ed. Brooks Cole, 1976.

[20] K. L. Kelly, E. Coronado, L. L. Zhao, and G. C. Schatz, “The Optical Properties of Metal Nanoparticles: The Influence of Size, Shape, and Dielectric Environment,” *J. Phys. Chem. B*, vol. 107, no. 3, pp. 668–677, 2003.

[21] C. F. Bohren, “How can a particle absorb more than the light incident on it?,” *Am. J. Phys.*, vol. 51, no. 4, p. 323, 1983.

[22] J. C. Venkata Reddy Nallagundla, Rakesh Lingam, *Handbook of Manufacturing Engineering and Technology*. 2015.

[23] D. M. Mattox, *Chapter 6 - Vacuum Evaporation and Vacuum Deposition*. 2010.

[24] M. Ohring, “Chemical Vapor Deposition,” in *Materials Science of Thin Films*, 2nd ed., vol. 2, San Diego: Academic Press, 2002, p. 277.

[25] S. M. George, “Atomic layer deposition: An overview,” *Chem. Rev.*, vol. 110, no. 1, pp. 111–131, 2010.

[26] H. Bruus, *Theoretical Microfluidics (Oxford Master Series in Physics)*, 1st ed., vol. 18. Oxford: Oxford University Press, 2007.

[27] K. R. Williams, K. Gupta, and M. Wasilik, “Etch Rates for Micromachining Processing - Part II,” *J. Microelectromechanical Syst.*, vol. 12, no. 6, pp. 761 – 778, 2003.

[28] C. E. Lyman, J. I. Goldstein, A. D. Romig, P. Echlin, D. C. Joy, D. E. Newbury, D. B. Williams, J. T. Armstrong, C. E. Fiori, E. Lifshin, and K.-R. Peters, “Basic SEM Imaging,” in *Scanning Electron Microscopy, X-Ray*

Microanalysis, and Analytical Electron Microscopy: A Laboratory Workbook, Springer, 1990, pp. 3–7.

[29] H. G. Tompkins and E. A. Irene, *Handbook of Ellipsometry*. New York: William Andrew, 2005.

[30] P. Colson, C. Henrist, and R. Cloots, “Nanosphere lithography: A powerful method for the controlled manufacturing of nanomaterials,” *J. Nanomater.*, vol. 2013, 2013.

[31] Y. Yu and G. Zhang, “Colloidal Lithography,” *Updat. Adv. Lithogr.*, vol. 8, pp. 3–34, 2013.

[32] G. Zhang and D. Wang, “Colloidal lithography - The art of nanochemical patterning,” *Chem. - An Asian J.*, vol. 4, no. 2, pp. 236–245, 2009.

[33] W. S. Rasband, “Image J,” *National Institutes of Health, Bethesda, Maryland, USA*. [Online]. Available: http://imagej.nih.gov/ij/. [Accessed: 15-Dec-2015].

[34] E. M. Larsson, C. Langhammer, I. Zorić, and B. Kasemo, “Nanoplasmonic probes of catalytic reactions.,” *Science*, vol. 326, no. 2009, pp. 1091–1094, 2009.

[35] H. Kim, “Characteristics and applications of plasma enhanced-atomic layer deposition,” *Thin Solid Films*, vol. 519, no. 20, pp. 6639–6644, 2011.

[36] P. Walker and W. H. Tarn, *CRC Handbook of Metal Etchants*, 1st ed. CRC Press, 1991.